


Quantum zero point electromagnetic energy difference between the superconducting and the normal phase in a high- T_c superconducting metal bulk sample

Annalisa Allocca,^{1,2,*} Saverio Avino,^{2,3} Sergio Balestrieri,^{1,4} Enrico Calloni,^{1,2} Sergio Caprara,^{5,6} Massimo Carpinelli,^{7,8} Luca D’Onofrio,^{1,2} Domenico D’Urso,^{8,9} Rosario De Rosa,^{1,2} Luciano Errico,^{1,2} Gianluca Gagliardi,^{2,3} Marco Grilli,^{5,6} Valentina Mangano,^{5,6} Maria Marsella,^{5,6} Luca Naticchioni,⁶ Antonio Pasqualetti,¹⁰ Giovanni Piero Pepe,^{1,2} Maurizio Perciballi,⁶ Luca Pesenti,^{8,9} Paola Puppo,⁶ Piero Rapagnani,^{5,6} Fulvio Ricci,^{5,6} Luigi Rosa,^{1,2} Carlo Rovelli,^{11,12,13} Davide Rozza,^{7,8} Paolo Ruggi,⁹ Naurang Saini,^{5,6} Valeria Sequino,^{1,2} Valeria Sipala,^{7,8} Daniela Stornaiuolo,^{1,2} Francesco Tafuri,^{1,2} Arturo Tagliacozzo ,^{1,2,14} Iara Tosta e Melo,^{7,8} and Lucia Trozzo²

¹Dipartimento di Fisica Ettore Pancini, Università degli Studi di Napoli Federico II, Via Cinthia, 80126-Napoli, Italy

²Istituto Nazionale di Fisica Nucleare, Sezione di Napoli, Via Cinthia, 80126-Napoli, Italy

³Consiglio Nazionale Ricerche-Istituto Nazionale di Ottica (CNR-INO), Via Campi Flegrei, 34, 80078-Pozzuoli, Italy

⁴Consiglio Nazionale Ricerche-Istituto ISASI, Via Pietro Castellino, 111, 80131-Napoli, Italy

⁵Dipartimento di Fisica, Università di Roma La Sapienza, Piazzale Aldo Moro, 2, 00185-Roma, Italy

⁶Istituto Nazionale Fisica Nucleare, Sez. Roma1, Piazzale Aldo Moro, 2, 00185-Roma, Italy

⁷Dipartimento di Fisica Giuseppe Occhialini, Università degli studi di Milano Bicocca, Piazza della Scienza 3, 20126-Milano, Italy

⁸Laboratori Nazionali del Sud, Istituto Nazionale Fisica Nucleare, Via Santa Sofia, 62, 95123-Catania, Italy

⁹Dipartimento di Scienze Chimiche, Fisiche, Matematiche e Naturali, Università di Sassari, Via Vienna, 2, 07100-Sassari, Italy

¹⁰European Gravitational Observatory - EGO, Via Edoardo Amaldi, 56021-Cascina, Italy

¹¹Campus of Luminy, Centre de Physique Theorique, Case 907, Marseille, F-13288, France

¹²Aix Marseille Université, Aix Marseille Université, CNRS, CPT, UMR 7332, Avenue Robert Schuman, Marseille, F-13288, France

¹³Université de Toulon, Université de Toulon, CNRS, CPT, UMR 7332, Avenue de L’Université, La Garde, F-83130, France

¹⁴CNR-SPIN, Monte S. Angelo via Cintia, 80126-Napoli, Italy



(Received 29 June 2022; revised 30 August 2022; accepted 16 September 2022; published 3 October 2022)

We provide a methodological approach to the estimate of the change of the quantum vacuum electromagnetic energy density in a high critical temperature superconducting metal bulk sample, when it undergoes the transition in temperature, from the superconducting to the normal phase. The various contributions to the Casimir energy in the two phases are highlighted and compared. While the transverse magnetic polarization of the vacuum mode allows for a macroscopic description of the superconducting transition, the changes in the transverse electric vacuum mode induced by the superconductive correlations are introduced within a microscopic model, which does not explicitly take into account the anisotropic structure of the material.

DOI: [10.1103/PhysRevB.106.134502](https://doi.org/10.1103/PhysRevB.106.134502)

I. INTRODUCTION

The electromagnetic (EM) field does work on each unit volume of matter at the rate $\vec{E} \cdot \vec{j}$, where \vec{E} is the electric field and \vec{j} is the charge current density. Feynman and coauthors, in their textbook on electromagnetism [1] stress the indefiniteness in the location of the EM field energy: “*It is sometimes claimed that this problem can be resolved by using the theory of gravitation ...all energy is the source of gravitational attraction.*” The Archimede project is designed for measuring the effects of the gravitational field on a Casimir cavity by performing a weighing measurement of the vacuum fluctuation force on a rigid Casimir cavity [2–4]. The vacuum state of the EM photon field is strongly modified in presence of a metal material, forming a coherent radiation-matter realm [5]. The goal of this project is to measure changes in the Casimir force when the cavity metal undergoes a phase transition from

the normal metal phase to the superconducting state. In the following we will address the two phases by talking shortly of a normal metal or a superconducting metal. There are speculations that the Casimir force can be the driving microscopic mechanism for superconducting pairing [6]. In this paper we adopt a more conservative view and assume that the largest contribution to the change in the Casimir force at the transition comes from modifications of the vacuum fluctuation spectrum due to changes in the photon field density of states at long wavelength, assuming that the thermodynamic free-energy gain at the transition (the so-called “condensation energy”) originates instead at atomic scale, by including short-distance lattice effects. The latter are considered as a small correction to the vacuum fluctuation spectrum and can be measured at very low temperature with a transition in magnetic field.

This work is devoted to the comparison in the Casimir energy between the normal and the superconducting phase of a metal slab considered as the Casimir cavity in free space. By choosing an high-temperature superconductor (HTS) as YBCO we gain various advantages. The transition

*Corresponding author: annalisa.allocca@na.infn.it

temperature is relatively high, which increases the feasibility of the experiment. We choose \hat{z} in the direction of the c axis orthogonal to the high- T_c superconductor planes, so that the collection of CuO planes are parallel to the planar surfaces of the material, thus exploiting the strong anisotropy of the superconducting correlations. The dominant contribution to the Casimir energy for a normal metal slab comes from the plasma modes that can be excited at the opposite surfaces. Retardation implies that they are both acoustic with a top frequency in the crossover between microwaves and infrared radiation (\sim THz), an energy range which is already rather high for a conventional superconductor. In spite of the fact that the electronic spectrum is not fully gapped in the superconducting phase, coherence of a HTS is expected to be more robust and preferable in this range of frequencies. Ignoring in this approach the nodes in the gap, YBCO has a maximum superconducting gap $\Delta \sim$ tens of meV which is in the same frequency range.

Differences arise between the superconductor and the normal phase because the minimal coupling of the EM field to the superconducting order parameter generates the Anderson-Higgs (AH) mechanism in the superconducting state [7–9]. The two transverse massless modes of the Maxwell equations in vacuum are replaced by three independent massive modes with mass $m^2 = (2\pi/\lambda_L)^2$ which, macroscopically, gives rise to the Meissner effect, i.e., the expulsion of the static magnetic fields from the superconducting bulk. This fixes an energy threshold for photon propagation inside the superconductor, given by $\hbar cm/n$, where n is the refraction index (denoted as Meissner threshold in the following). While the superconducting correlation length ξ can be of the size of the sample, the Meissner penetration length is relatively small in the c -axis direction $\lambda_L^{\perp, \text{YBCO}} \sim 0.75 \mu\text{m}$, where λ_L is the London penetration length. The latter is of the order of the skin depth in the normal metal, at least for a pure sample. However, the transverse electric (TE) vacuum modes, characterized by E_z penetrating in the sample, perform in any case very differently between the two phases as for what concerns the interaction with the surface plasma excitations. Resonant tunneling below the Meissner threshold, assisted by virtual quasiparticle (QP) electronic excitations is still possible if the slab has thickness $a \gtrsim 2\lambda_L$, as will be explained in the following.

For a macroscopic metal body of linear millimeter size a , in coherence with the EM vacuum, a macroscopic approach is usually adopted, resorting to a semiclassical response theory in terms of a dielectric function $\epsilon(\omega)$ (intended at $k \approx 0$ for an isotropic system). A macroscopic description of the transverse magnetic (TM) photon vacuum in the presence of a slab-like cavity is allowed as the TM modes have $B_z = 0$ which can be macroscopically compatible with the metal both in the normal and superconducting phases. Indeed, superconductors require $B_z = 0$ at the boundary with the plane surface due to Meissner effect. Among the nonvanishing field components (E_x , E_z , and B_y), the $\epsilon(\omega)E_z$ component should be matched at the boundary. In a slab geometry $\epsilon(k_{\parallel}, \omega)$ entails plasma surface modes ($k_{\parallel} \parallel a$ - b planes) coupled between the two opposite surfaces, which can be classified as symmetric plasma mode (SPM) and antisymmetric plasma mode (ASPM) with respect to the inversion plane of the slab. Only the transverse magnetic

(TM) photons couple to these modes. It is well known that in the normal metal the SPM and the ASPM give opposite, almost compensating, contributions to the Casimir energy and the ASPM prevails with its minus sign [10]. We will argue that the superconductor has collective modes corresponding to the SPM and ASPM, the Mooij-Schön (MS) mode, and the Carlson-Goldman (CG) mode, respectively. On the other hand, in the superconducting phase the MS mode is a true plasma oscillation mode, while the CG one is macroscopically charge neutral, balancing a QP electron component with a Cooper pair component which, in the case of nodes in the gap, does not require too much energy. The CG mode being neutral does not couple macroscopically to the zero point extended TM photons, thus implying the absence of compensation occurring in the normal phase, which makes a sizable difference when comparing the results of the two phases in first approximation. Moreover, in the superconducting phase, the two transverse massive modes are both similar to TM modes and they both couple to the MS excitation mode.

The TE mode (which is characterized by nonzero B_x, B_z, E_y components) does not couple to the plasmonic surface excitations in the normal metal, at least in a macroscopic approach based on a Drude-type frequency-dependent dielectric constant $\epsilon(\omega)$. In the superconducting case, the longitudinal AH massive photon mode is similar to a TE mode and we expect that it does not couple with the MS plasmon, either. On the contrary, it allows for longitudinal resonant states to arise, which split off the minimum of the AH band in the confined geometry, provided Cooper pairs can be, even just virtually, broken. These pair-broken states couple with the B_z component of the incoming AH mode. However, to describe this physics, the macroscopic picture cannot be adopted. In fact, the B_z component of the longitudinal, so called, TE mode would violate the macroscopic London $B_z = 0$ boundary condition for the superconductor. A realistic model accounting for the full microscopic electronic structure of the real sample is beyond any possible approach. The idea is to replace the actual cavity with an effective local interaction between the nonvanishing B_z component and pair breaking in the a - b planes. For YBCO the Meissner threshold is of the order of the gap Δ , so that the resonant state can be located in the coherent subgap energy window. We will adopt a two-channel scattering approach for the TE mode by considering virtual photon emission or absorption processes, as the result of the interaction of the incoming wave with quasiparticles close to the nodes of the gap. We will show that resonant states arise in the case of normal incidence of the TE mode onto the film surfaces.

In Sec. II we present the macroscopic approach for deriving the contribution to the Casimir energy from interaction of the TM mode with the surface plasma waves for various linear lengths of the sample which plays the role of the Casimir cavity. Section II A discusses the case of a normal medium, while Sec. II B is devoted to the superconducting medium. The ideal normal metal is characterized by a single parameter, the plasma frequency ω_p . Hence, the length scale is c/ω_p where c is the propagation velocity in the material. According to London theory, ω_p is replaced in the superconducting phase by the superconductive plasma frequency $\omega_{ps} = (4\pi n_s e^2/m)^{1/2}$, in which the density of Cooper pairs

n_s appears replacing the electron density n . Here c/ω_{ps} is the London penetration length λ_L for an isotropic medium. This implies that close to the transition temperature the normal and the superconductive length scales are quite different, while for temperatures not in the transition region the two scales can be considered as being roughly equal. In Sec. III we will present the effective model for the microscopic model approach of a TE mode characterized by the B_z field component propagating at normal incidence. Details are given in Appendixes A and B. Section IV is devoted to the Casimir energy of the superconducting phase. Further scattering features of the model, including phase-shift jumps, are critically analyzed. The total Casimir energy for the two phases and their difference is presented in Sec. V. Section VI includes a summary and the conclusions that can be extracted which could be useful in the interpretation of the experiment.

Keep in mind, any time we discuss qualitative physics related to superconductors we assume zero temperature and ignore the fact that HTS materials, YBCO in particular, are strongly anisotropic and that there are nodes in the d -wave excitation gap. In this sense, the gap is 2Δ with no QP's in this energy range both in the text and in the pictures. Also, the velocity of light is denoted as c with no care of the refractive index. These simplifications aim to highlight the differences of the superconducting phase with respect to the normal phase. We are aware, of course, that quantitative analysis would require to include these peculiarities of the HTS carefully, and we mention and introduce them in the text and in the numerical estimates, when they cannot be overlooked.

The approach considered in this paper explicitly uses the bulk behavior of the superconductor, while in the case of the experiment one can consider both the use of bulk samples and thin films, and also the superposition of thin layers [11]. In this sense, it is expected to extend this work to the limiting case of thicknesses tending to zero, in the nanometer limit.

II. COMPARISON BETWEEN THE NORMAL AND THE SUPERCONDUCTING PHASE ENERGY SCALES

To compare the superconducting and the normal phases of our sample from the macroscopic point of view, we have to define the dielectric properties of the two phases with the energy scales involved.

In the case of the normal phase, when the inelastic scattering time τ is long enough (i.e., in the limit $\omega\tau \gg 1$), we can assume that the sample is close to be an ideal metal. With the TM polarization, E_z penetrates inside the metal over a length δ named "skin penetration depth." The Drude conductivity for the ideal normal metal σ , of real part σ_1 and imaginary part σ_2 , can be used:

$$\sigma = \frac{ne^2}{m} \frac{1}{1/\tau - i\omega} \rightarrow \sigma_2(\omega) = \sigma_0 \frac{\omega\tau}{1 + \omega^2\tau^2}$$

(with $\sigma_0 = ne^2\tau/m$) allows to define a frequency scale:

$$\omega_0 = \frac{c}{\delta} = c \sqrt{\frac{4\pi}{c^2} \sigma_2(\omega_0)} \omega_0 = 4\pi \sigma_2(\omega_0). \quad (1)$$

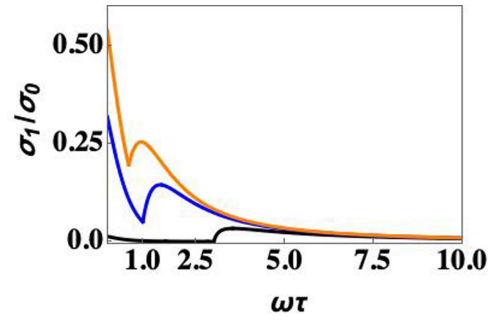


FIG. 1. σ_1 vs $\omega\tau$ for $\Delta\tau = 1.5$ (lowest curve), 0.5, 0.3 and $k_B T \tau = 0.3$. τ is the inelastic scattering time.

For the ideal normal metal, Eq. (1) recovers $\omega_p = \sqrt{4\pi ne^2/m}$, the normal metal plasma frequency.

With the chosen geometry, the nodal lines of the d -wave order parameter for high- T_c superconductors lie in the a - b plane parallel to the surfaces of the material. Although the nodes of the gap Δ imply that some density of QP's is excited even at $T \approx 0$, we consider the gap Δ quite robust for transport in the c direction. In Fig. 1 we report the real part of the conductivity, σ_1 , at finite frequency, at $\vec{q} = 0$ (i.e., its bulk value), for increasing Δ at fixed temperature for an s -wave superconductor, as derived from Ref. [12]. When $k_B T \ll \Delta$, σ_1 is quite small at frequencies $\omega < 2\Delta$, except for the pseudo-Drude peak at zero frequency, which contributes to the sum rule $\int_0^\infty d\omega 4\pi\sigma_1(\omega) = \pi\omega_{ps}^2/2$ in the limit $\tau \rightarrow \infty$ and is not included in the plot. This implies that the Kramers-Kronig transform for σ_2 ,

$$\sigma_2(\omega) = -\frac{\omega}{\pi} \int_{-\infty}^{\infty} d\omega' \frac{\sigma_1(\omega')}{\omega'^2 - \omega^2}, \quad (2)$$

is dominated mostly by the enhancement of excitations close to the pair-breaking energy, but also by the zero-frequency peak. Including just the latter δ peak, we obtain

$$\sigma_1 \ll \sigma_2 \sim \frac{n_s e^2}{m\omega}, \quad (3)$$

where n_s is the Cooper pair density. Hence, the polarizability is quite high at microwave frequencies [13]

$$\epsilon_1(\omega) \approx -4\pi\sigma_2/\omega \quad (4)$$

in the limit $\tau \rightarrow \infty$. It follows that the superconducting dielectric function is not much different from the normal one, except for frequencies close to the pair-breaking energy $2\Delta/\hbar$, where it has an enhancement just above the gap threshold [14]. The main differences are expected in the quantitative energy scale of the modes and in their lifetime [15–18]. A plot of an approximation of the real part $\epsilon_1(\omega)$ for the superconducting and normal phases is displayed in Fig. 2.

In the superconducting case, inserting Eq. (3) in Eq. (1) we obtain the superconducting plasma frequency $\omega_{ps} = \sqrt{4\pi n_s e^2/m}$. As expected, the definition of Eq. (1) appears convincing on the full range normal \leftrightarrow superconductor, when screening is low. In the case of YBCO, the anisotropy of the London length is important as $\lambda_L^\perp/\lambda_L^\parallel = 5$ (where λ_L^\parallel is in the a - b plane). With the choice $\omega_{ps} = \frac{c}{\sqrt{\epsilon_s}\lambda_L^\perp}$, which is valid in the limit $\omega\tau \gg 1$, and with $\epsilon_s = 30$, $\lambda_L^\perp \sim 0.75 \mu\text{m}$,

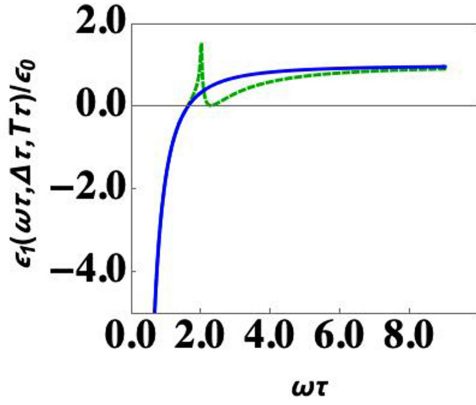


FIG. 2. Comparison between $\epsilon_1(\omega\tau, \Delta\tau, T\tau)$ of the normal ideal metal case $\epsilon_1(\omega\tau, 0, T\tau) = 1 - 2.6/(\omega\tau)^2$ (full blue curve) and for the superconducting case $\epsilon_1(\omega\tau, \Delta\tau, T\tau)$ (green dashed curve) vs $\omega\tau$. Here $\Delta\tau = 1.0$ and $T\tau = 2.0$ (with $\sigma_0 = 0.7$). The sharp peak at $\omega \sim 2\Delta/\hbar$ heralds the enhancement of QP excitations at the pair-breaking energy. Difference between the two curves is only close to $\omega \sim 2\Delta/\hbar$.

which gives $\omega_{ps} \sim 0.7 \times 10^{14}$ Hz = 48 meV. The maximum gap for YBCO is $\Delta \sim 16$ meV, so that $2\Delta < \omega_p$, but rather close to it.

III. PHOTON MODES IN INTERACTION WITH THE METAL FILM

A. TM polarization: Contribution of the plasma modes to the Casimir energy, in the normal metal phase

Let us now introduce the Maxwell equation outside of the superconductor and the boundary conditions:

$$\left(\nabla^2 + \mu\epsilon \frac{\omega^2}{c^2}\right) \begin{Bmatrix} \vec{E} \\ \vec{B} \end{Bmatrix} = 0. \quad (5)$$

The modes have dispersion $\frac{\omega^2}{c^2} = k_{\parallel}^2 + k_z^2$. As the TM mode has $B_z = 0$, it can be macroscopically compatible with the metal both in the normal and in the superconducting phases. Indeed, superconductors require $B_z = 0$ at the boundary with the plane surface. Among the nonvanishing field components (E_x , E_z , and B_y), continuity of $D_z = \epsilon(\omega)E_z$ is required, assuming vanishing charge density at the surface. These conditions, written for the TM mode component E_z across a single vacuum-material boundary, are

$$\epsilon_L(\omega) \Phi_L - \epsilon_R(\omega) \Phi_R = 0, \quad \Phi'_L - \Phi'_R = 0 \quad (\text{TM}), \quad (6)$$

where L is the vacuum at the left-hand side, with $\epsilon_L = \epsilon_0 = 1$, and R is the material at the right-hand side with dielectric function $\epsilon_R(\omega)$. Here the prime denotes derivative. At microwave frequencies, the electric field penetrates into the bulk of the normal material over the skin depth [19], which is of the order of the London penetration length at these frequencies. Bound states at surfaces $z = 0$ and $z = a$ imply

$$\Phi = \begin{cases} A e^{\kappa_0 z}, & z < 0 \\ B e^{-\kappa_a z} + C e^{-\kappa_a(a-z)}, & 0 < z < a \\ D e^{-\kappa_0 z}, & a < z \end{cases} \quad (7)$$

with

$$\Rightarrow \epsilon_{a/0}(\omega) \frac{\omega^2}{c^2} = k_{\parallel}^2 - \kappa_{a/0}^2, \quad (8)$$

where the subscript a refers to the $0 < z < a$ space region, while the subscript 0 is for the vacuum regions. Assuming inversion symmetry at $a/2$ is $C = \pm B$ and $D = \mp A$. Hence, Eq. (6) at $z = 0$ becomes

$$\begin{cases} B[-\kappa_a \pm \kappa_a e^{-\kappa_a a}] - A \kappa_0 = 0, \\ \epsilon(\omega) B[1 \pm e^{-\kappa_a a}] - A = 0. \end{cases}$$

The requirement $\det_{\mp} = 0$ implies

$$-\frac{\kappa_a}{\kappa_0} [1 \mp e^{-\kappa_a a}] = \epsilon_a(\omega) [1 \pm e^{-\kappa_a a}]. \quad (9)$$

In the case of no retardation and ideal metal, the two plasma modes are very simple. No retardation ($c \rightarrow \infty$) implies $\kappa_a = \kappa_0 = k_{\parallel}$. Adopting the Drude form for $\epsilon_a(\omega) = 1 - \omega_p^2/\omega^2$ where $\omega_p^2 = 4\pi n e^2/m$ is the plasma frequency for electronic density n , electron charge e and mass m , we get

$$\det_+ = 0 \Rightarrow \omega_+^2 = \frac{\omega_p^2}{1 + \coth\left(\frac{k_{\parallel} a}{2}\right)} \quad (10)$$

for the symmetric plasmon and

$$\det_- = 0 \Rightarrow \omega_-^2 = \frac{\omega_p^2}{1 + \tanh\left(\frac{k_{\parallel} a}{2}\right)} \quad (11)$$

for the antisymmetric plasmon. $\omega_+(k_{\parallel} a)$ is an acoustic mode and is rather unchanged when retardation is included, while $\omega_-(k_{\parallel} a)$ is strongly modified by retardation.

Defining $f_{\pm}[x] = \coth[x]$ ($f_{-}[x] = \tanh[x]$) the total energy associated to each plasma mode is as follows: We now integrate on k_{\parallel} ,

$$\begin{aligned} \mathcal{E}_{\pm}^{\text{TM}} &\equiv \frac{1}{2} \sum_{k_{\parallel}} \omega_{k_{\parallel}}^{\pm} \\ &= \frac{1}{2} \frac{L^2}{(2\pi)^2} \int_0^{+\infty} 2\pi k_{\parallel} dk_{\parallel} \frac{\omega_p}{\sqrt{1 + f_{\pm}\left[\frac{k_{\parallel} a}{2}\right]}} \end{aligned} \quad (12)$$

or, with $k_{\parallel} L = x$,

$$\begin{aligned} \mathcal{E}_{\pm}^{\text{TM}} &\equiv \frac{\omega_p}{2\pi} \int_0^{+\infty} x dx \frac{1}{\sqrt{1 + f_{\pm}\left[\frac{ax}{2L}\right]}} \\ &= \frac{\omega_p}{2\pi} \left(\frac{2L}{a}\right)^2 \frac{1}{2} \left\{ - \int_0^{+\infty} dy \frac{y^2}{2} \frac{\partial}{\partial y} \frac{1}{\sqrt{1 + f_{\pm}[y]}} \right\}. \end{aligned} \quad (13)$$

To include retardation, we define $\kappa = \sqrt{k_{\parallel}^2 - \frac{\omega^2}{c^2} \epsilon(\omega)}$ and use $\lambda = a \frac{\omega_p}{c}$, $s = k_{\parallel} a$, $v = \frac{\omega}{\omega_p}$:

$$0 = \det_{\pm} = \sqrt{\frac{s^2 + \lambda^2(1 - v^2)}{s^2 - \lambda^2 v^2}} + \left(1 - \frac{1}{v^2}\right) f_{\pm} \left[\frac{\sqrt{s^2 + \lambda^2(1 - v^2)}}{2} \right]. \quad (14)$$

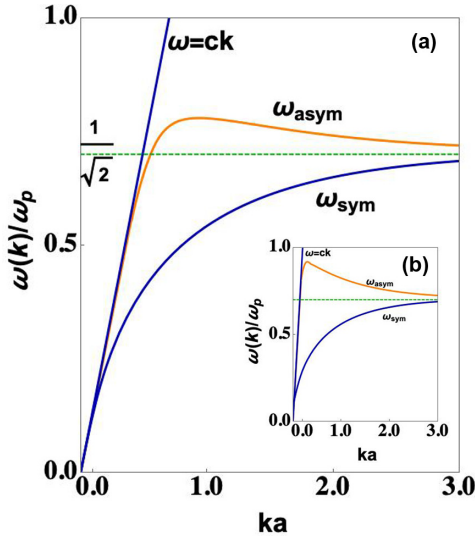


FIG. 3. The symmetric (ω_{sym}) and antisymmetric (ω_{asym}) dispersion relation for the plasma bound excitations vs k_{\parallel} (with $k_{\parallel} > \frac{\omega}{c}$), in the retarded normal case, for two different linear sizes of the sample $a\omega_p/c = 0.7$ (a) and $a\omega_p/c = 0.2$ inset (b). The linear light dispersion $\omega = ck$ has also reported in the corresponding scale. The dashed green line is the asymptotic limit at $\omega_p/\sqrt{2}$.

Solutions are only for $s > \lambda v \rightarrow k_{\parallel} > \omega/c$. This limitation guarantees that they are bound states (decaying outside the slab). At very small s , v has to be also very small to keep the square root real. This implies that $(1 - \frac{1}{v^2})$ is strongly negative and a solution is always found for both equations. $v_{\pm}(s)$ is the solution of $\det_{\pm}(s, v, \lambda) = 0$ and is given in Fig. 3 for $\lambda = 0.7$ [Fig. 3(a)] and 0.2 [Fig. 3(b), inset]. The function $\det_{\pm}[s, v, \lambda]$ depends on a . Dropping the label \pm for simplicity we get

$$\mathcal{E}^{\text{TM}} \equiv \frac{1}{2} \sum_{k_{\parallel}} \omega_{k_{\parallel}} = \frac{\omega_p}{2\pi} \left(\frac{2L}{a} \right)^2 \times \frac{1}{2} \left\{ - \int_0^{+\infty} ds \frac{s^2}{2} \int dv \frac{\partial v}{\partial s} \delta[v - v(s)] \right\}. \quad (15)$$

Here $\frac{\partial v}{\partial s} = - \frac{\partial \det}{\partial s} / \frac{\partial \det}{\partial v} |_{\lambda}$.

For the case $a\omega_p/c = 0.2$ we have

$$\begin{aligned} \mathcal{E}_{\alpha}^{\text{TM}} &\equiv \eta_{\alpha} \times \frac{\omega_p}{2\pi} \left(\frac{2L}{a} \right)^2, \\ \eta_{-}^{\text{ret}} &\approx 0.157931, \\ \eta_{+}^{\text{ret}} &\approx -0.204317 \end{aligned} \quad (16)$$

(label $\alpha = \mp$ stands for antisymmetric and symmetric, respectively) to be compared with the nonretarded ones from Eq. (13), $\eta_{-}^{\text{nonret}} \approx 0.167578$, $\eta_{+}^{\text{nonret}} \approx -0.192115$. While the energy dispersion $\omega_{-}(k_{\parallel})$ is quite different for small k_{\parallel} and becomes acoustic for both modes in the retarded case, the difference in their contribution to the Casimir energy, per unit cross-section area L^2 is rather small. This is shown in Fig. 4 for various linear widths of the sample $z = ac/\omega_p$. E_{\pm} and their sum $E_{+} + E_{-}$ (black dots) are reported vs ac/ω_p . The

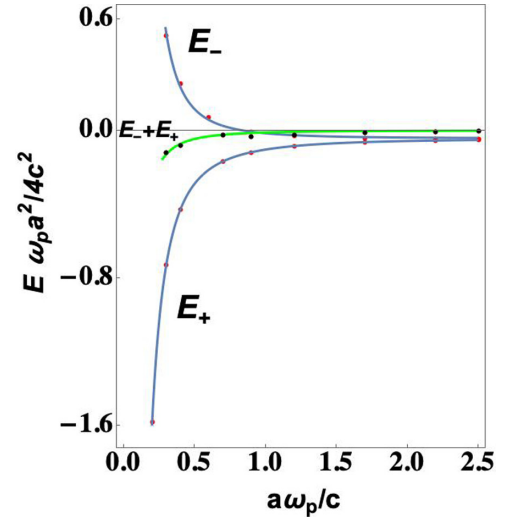


FIG. 4. Contribution to the Casimir energy, per unit area L^2 , for various linear sizes ac/ω_p , coming from the plasma modes in the normal ideal metal sample. E_{+} (E_{-}) comes from the symmetric (antisymmetric) plasma mode. The full blue curves are fits of the red dots with $z^{-\alpha}$, where $\alpha \approx \frac{5}{2}$ for E_{-} and $\alpha \approx 2$ for E_{+} . E_{-} is negligible beyond $dc/\omega_p \sim 1$. The black dots correspond to the sum $E_{+} + E_{-}$. The fit green curve is a power law just weaker than z^{-3} (see Sec. III D).

fitting of the sum $E_{+} + E_{-}$ (green curve) gives a scaling law close to z^{-3} but weaker (see discussion in Sec. III C).

B. TM polarization: Plasma excitations in the superconducting phase

Because of the presence of the gap Δ in the spectrum, it can be argued that the plasma modes are much better defined in the superconducting case than in the normal phase. In fact, with the exclusion of the nodes of the energy excitation spectrum, in the rest of the two-dimensional (2D) Brillouin zone, they are located in the energy gap. In the case of the TM mode, continuity of $\epsilon(\omega)E_z$ at the boundary with exponential decay inside the sample provides the energy dispersion of the plasma modes.

The plasma mode dispersions for a superconducting film have been plotted with a “phenomenological” approximation in Ref. [20] and they do not look much different from our Fig. 3, except for the frequency scale which replaces the normal metal plasma frequency ω_p with the superconducting one ω_{ps} (the 2D mode dispersion implies in both cases an extra factor $1/\sqrt{2}$). Similarly to the normal case of Fig. 3 the symmetric and antisymmetric modes of Ref. [20] are $\sim \sqrt{k_{\parallel}}$ and $\sim 1/\sqrt{k_{\parallel}}$, respectively. However, the similarity is conceptually misleading. In the case of Ref. [20], the film is embedded in a nonconducting medium with an enormous value for the static dielectric constant ($\bar{\epsilon} \sim 2 \times 10^4$). The phase velocity of Ref. [20] is $\omega/k_{\parallel} < c/\sqrt{\bar{\epsilon}}$, so that a frequency-independent retardation approach can be adopted. This is equivalent to ignore retardation which is mostly relevant in our case, as the film is located in vacuum and the bulk plasma frequency $\omega_{ps} \gtrsim 2\Delta$, or even $\lesssim 2\Delta$. More generally, we can estimate the scale of the dispersion ω_0 for YBCO as $\omega_0 = R_{\text{sq}}/L$ where R_{sq} is the

sheet resistance in the nonsuperconducting state ($\sim 2 \times 10^{-4} \Omega$ at ~ 10 GHz) and L is the kinetic inductance (expected to be much larger than the geometric inductance) (with dimensions Ω s and Ω is Ohm). In the case of an s -wave superconductor, the commonly used expression [21] is

$$L \approx \frac{R_{sq} \hbar}{\pi \Delta} \frac{1}{\tanh\left(\frac{\Delta}{2k_B T_c}\right)}. \quad (17)$$

Adopting this definition for L , and a BCS form for $\xi \sim 10$ nm, we get

$$\omega_0 \sim \frac{v_F}{\xi} \sim 10^{14} \text{ s}^{-1}. \quad (18)$$

In the limit $\omega\tau \gg 1$ (the (inductance per unit length) $^{-1}$ for a sample of $1 \mu\text{m}$ length can be estimated as $n_s e^2/m \sim 10^{19} (\Omega \times \text{s})^{-1}$, which produces the same order of magnitude for ω_0 as Eq. (18).

Mooij and Schön [22] (MS) derived the collective excitation modes in reduced geometries from a hydrodynamical approach for charge imbalance. In a superconducting wire of diameter r_0 a linear dispersion mode is well defined for $kr_0 \ll 1$, with velocity $c_{pp}^2 \approx \omega_{ps}^2 \frac{r_0^2}{2} \epsilon_s^{-1} \ln(1/kr_0)$, where ϵ_s is the dielectric constant in the superconducting phase. They also remark that, in the case of a superconducting slab of thickness d in vacuum, the screening voltage is $\delta V(x, r)$ with r in the surface plane. The 2D Fourier transform is $\delta V = \frac{2\pi}{k} \tilde{\sigma}$, where $\tilde{\sigma} = \delta\rho_s d$ is the induced surface charge density ($\delta\rho_s$ is the volume-induced charge and d is the thickness of the slab in the third direction). The three-dimensional (3D) Fourier transform is $\delta V = \frac{4\pi}{k^2} \rho$, so that we have

$$\delta V(k, a) = \frac{2\pi}{k} \left[\frac{a}{\epsilon_s} + \frac{2}{k} \right] \delta\rho_s. \quad (19)$$

The continuity equation for the superconducting-induced charge with $\dot{\rho}_s = -i\omega F \rho_s$ and $F = 1 + 2\epsilon_s/(ka)$ given by Eq. (19), together with Euler equation, provides

$$(\omega^2 + i\omega\tau_{\text{imp}}^{-1})F(k_{\parallel}) = \omega_0^2. \quad (20)$$

Keeping just the real part, in the limit $ka \ll 1$ we have

$$\omega^2 \frac{2\epsilon_s}{k_{\parallel} a} = \omega_0^2 \Rightarrow \omega^2 = \frac{\omega_0^2 a}{2\epsilon_s} k_{\parallel} \quad (21)$$

which is the MS acoustic mode for a slab, with $\omega \propto \sqrt{k_{\parallel}}$ (Fig. 5). It follows the k_{\parallel} dependence is the same as of the symmetric plasma mode of the normal phase of Fig. 3 and of the symmetric one in Ref. [20], though not in scale. It is reasonable to assume that $\omega'_0 \sim \omega_0$ given in Eq. (18), so that the prefactor in the dispersion of Eq. (21) is of the order of

$$\sqrt{\frac{\omega_{ps}^2 a}{2\epsilon_s}} \sim 0.07\text{--}0.3 \times 10^{14} \text{ m}^{1/2}/\text{s}, \quad (22)$$

for $\omega_{ps} \sim 0.7 \times 10^{14} \text{ Hz} = 46 \text{ meV}$. The upper threshold for the MS acoustic mode is $\omega_0 < 2\Delta \lesssim \hbar\omega_{ps}$.

The mode corresponding to the ASPM is most probably the Carlson-Goldman (CG) mode, which is close to the pair-breaking energy and involves charge compensation between the charge modulation of the pair condensate and the charge modulation of the QP's. At low temperatures, the CG velocity

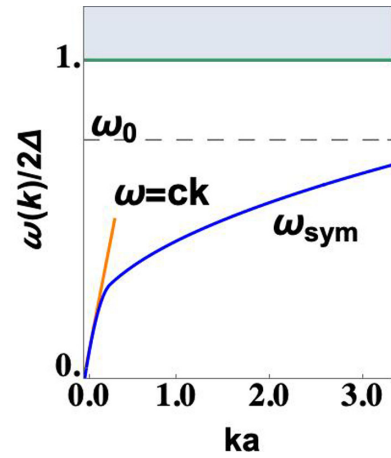


FIG. 5. The dispersion of the symmetric Mooij-Schön mode ($\propto \sqrt{k}$) in a superconducting film. Vertical axis not in scale.

is c_{CG} :

$$c_{\text{CG}}^2 = \frac{n_s}{m} \frac{1}{2N(0)} \approx \frac{n_s}{n} \frac{1}{6} v_F^2 \quad (23)$$

[$N(0)$ is the density of states at the Fermi energy]. It is expected to be quite short lived, particularly at small k_{\parallel} . Besides, being this mode charge neutral, it does not couple, at first order, with the photon of the EM vacuum. The signature of the pair-breaking processes in the dielectric function appears at about $k_0 = \frac{2\Delta}{\hbar v} \sim 250 (\mu\text{m})^{-1}$, as discussed in Appendix C. This k vector refers to sampling distances of the order of the lattice spacing, beyond the validity of our approach.

To sum up the case of the TM modes, our conclusion is that, in first approximation, the CG neutral mode which corresponds to the ASPM in the normal metal case does not contribute to the Casimir energy because it does not couple to the zero-point photon field. The SPM instead grows linearly with k_{\parallel} at low k vectors and bends as $\sqrt{k_{\parallel}}$, not different from the normal ideal metal, but with an energy scale which is different from the normal case, given by Eq. (18). The SPM contributes to lower the Casimir energy. In the superconducting case here is no subtraction of the positive contribution given by the ASPM, as it happens for the normal metal TM case. In the next section we discuss the TE case for the superconducting metal, in which resonant propagating modes may be present below the AH threshold.

C. Total Casimir energy in the normal phase

An estimate of the Casimir energy for the normal phase of the sample requires the full density of states of the photon propagating modes at energies which correspond to the Meissner window of the superconducting phase. These energies contribute to the total Casimir energy difference, from the normal phase side. A tutorial approach to this contribution can be envisaged by adopting a simple model for the transmission across the sample. In this case a single elastic channel suffices because QP's in the metal only contribute to the propagation with a finite lifetime. Following Bordag [10], we mimic the cavity as in Sec. IV, with two δ -function potentials at the distance $2d$. The zero-point energy of a photon of wave vector

$K = \sqrt{|k_{\parallel}^2 + k^2|}$ and energy $\frac{1}{2}\hbar cK$, where c is the velocity of the incoming and outgoing photons in the vacuum. Scattering is assumed to be elastic. The strength of the δ functions is tuned by the inverse decaying length κ of the field. We anticipate here some results of a two-channel scattering model that is presented in Sec. IV B. The total transmission is

$$\begin{aligned}
 t(k_{\parallel}, k) &= \frac{e^{i(k-q)d}}{1 + \frac{t_R}{t_L} r_R^* r_L e^{2iqd}} \\
 &\rightarrow \frac{1}{\left(1 - \frac{k_{\parallel}^2}{k^2} + \frac{ik}{2k}\right)^2} \frac{e^{i(k-q)d}}{1 - \frac{\kappa^2}{4k^2} \frac{1}{\left(1 - \frac{k_{\parallel}^2}{k^2} + \frac{ik}{2k}\right)^2}} e^{2iqd}, \quad (24)
 \end{aligned}$$

where k is the k vector in the \hat{z} direction out of the scattering region and q is the corresponding k vector between the two barriers (we take $q = k$). t_i (r_i) ($i = R, L$) are the transmission (reflection) coefficients of the two δ potentials which we have chosen equal. This can also be derived restricting the matrix S_{12} of Eq. (40) to a single channel. The total-energy contribution coming from these delocalized states is [23]

$$\begin{aligned}
 E_{\text{tot}}^n &= \frac{1}{2} \sum_{k_{\parallel}} \omega_{k_{\parallel}}^{\text{TM}} + \frac{L^2}{2} \int \frac{2\pi k_{\parallel} dk_{\parallel}}{(2\pi)^2} c \sum_{\alpha} \\
 &\times \sqrt{\frac{\omega_{\alpha}^2}{c^2} + k_{\parallel}^2 - \epsilon(\omega_{\alpha}) \frac{\omega_{\alpha}^2}{c^2}} \left[\frac{\partial}{\partial k} \ln \frac{t(k_{\parallel}, k)}{t(k_{\parallel}, -k)} \right] \Big|_{\omega_{\alpha}}. \quad (25)
 \end{aligned}$$

$\omega_{k_{\parallel}}^{\text{TM}}$, the plasma energy modes in the first term, arise from the poles of $t(k_{\parallel}, k)$. ω_{α} are the eigenvalues of the operator $-\frac{d^2}{dz^2} + V(z)$ arising from the Schrödinger equation of the potential in the z direction. The ratio $\frac{t(k_{\parallel}, k)}{t(k_{\parallel}, -k)} = e^{2i\delta}$ where δ is the phase shift in the transmission. To subtract non-distance-dependent terms from the expression of Eq. (25), we substitute $t \rightarrow t/t_{d=\infty}$. As the approach is only qualitative, we rewrite it in the continuum limit $\omega_{\alpha} = ck$. We get

$$\begin{aligned}
 E_{\text{tot}}^n &= \frac{1}{2} \sum_{k_{\parallel}} \omega_{k_{\parallel}}^{\text{TM}} + \frac{L^2}{2} \int \frac{2\pi k_{\parallel} dk_{\parallel}}{(2\pi)^2} c \\
 &\times \int_0^{+\infty} \frac{dk}{2\pi i} \sqrt{|k_{\parallel}^2 + k^2|} \frac{\partial}{\partial k} \ln \frac{t(k_{\parallel}, k)}{t(k_{\parallel}, -k)}. \quad (26)
 \end{aligned}$$

By Cauchy theorem the k integration can be performed along the imaginary axis $k \rightarrow ik$ and the deformation of the circuit shows that this integral already includes the residues at the plasma poles, so that the integral along the imaginary axis provides the full contribution to the Casimir energy. Integrating by parts, we obtain

$$\begin{aligned}
 E_{\text{tot}}^n &= -\frac{L^2}{2} \int \frac{2\pi k_{\parallel} dk_{\parallel}}{(2\pi)^2} \\
 &\times c \int_0^{+\infty} \frac{dk}{\pi} \frac{k}{\sqrt{|k_{\parallel}^2 - k^2|}} \ln \left[\frac{1}{1 - \left(\frac{\frac{\kappa k}{2}}{k_{\parallel}^2 - k^2 - \frac{\kappa k}{2}}\right)^2 e^{-2kd}} \right]. \quad (27)
 \end{aligned}$$

When $k_{\parallel} \gtrsim \kappa$, $t(k_{\parallel}, k)$ of Eq. (24) has three poles with increasing k , which qualitatively reproduce the crossings with

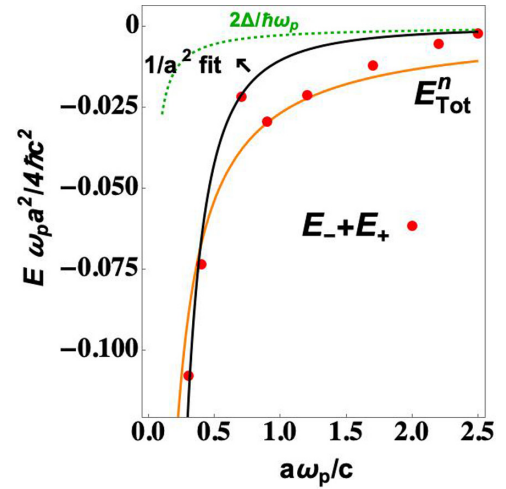


FIG. 6. Total energies per unit surface $E_+ + E_-$ of Fig. 4 (red dots) and E_{tot}^n evaluated at $\kappa d = 0.05$ vs the linear size of the sample $z = a\omega_p/c$ (orange curve). E_{tot}^n scales with the linear size of the sample as z^{-3} and has been shifted to match with $E_+ + E_-$ at $z = 1.0$. The weight of the change in the density of states due to the propagating states increases at larger a values. A fit $E a^2 \sim 1/a^2$ (black curve) has been added as well as the pair-breaking threshold $2\Delta/\omega_p$ in the superconducting phase, for comparison (green dotted curve).

the SPM curve, the ASPM, and the light dispersion curve $\omega = ck_{\parallel}$. Their contribution to the integral is negative, positive, and negative, respectively, as expected, but there is no correspondence of the location in energy with the dispersion laws of Fig. 3. Rewriting Eq. (27) in dimensionless variables, $s' = 2kd$, $s = 2k_{\parallel}d$, $\kappa' = \kappa d$, Eq. (27) becomes, with $4d = a$,

$$\begin{aligned}
 E_{\text{tot}}^n &= -\frac{1}{2} \left(\frac{2L}{a}\right)^2 \frac{\omega_p}{2\pi} \times \frac{2}{\pi} \frac{c}{\omega_p a} \int s ds \\
 &\times \int ds' \frac{s'}{\sqrt{|s^2 - s'^2|}} \ln \left[\frac{1}{\left| 1 - \left(\frac{\kappa' s'}{s^2 - s'^2 - \kappa' s'}\right)^2 e^{-s'} \right|} \right] \quad (28)
 \end{aligned}$$

to be compared with Eq. (13). The $\sim z^{-3}$ dependence on the linear widths of the sample $z = ac/\omega_p$ is apparent. At very small κ' 's, the transmission is close to unity for $k_{\parallel} = 0$ and we expect that E_{tot}^n is roughly given by the plasma modes contribution only. It follows that E_{tot}^n should be very close to the behavior of $E_+ + E_-$ plotted in Fig. 4 (red dots and green line). A numerical evaluation of the double integral at $\kappa d = 0.005$ gives 0.0075 and E_{tot}^n does not match with $E_+ + E_-$ at small $z = a\omega_p/c$. However, the two derivations stem from different approaches and it is not of a surprise that the two results do not match. As the present approach cannot be considered quantitatively faithful, we scale E_{tot}^n at $\kappa d = 0.005$ to make it coincide with $E_+ + E_-$ at $z = 1.0$. In Fig. 6, $E_+ + E_-$ vs z is reported (red dots), together with $E_{\text{tot}}^n \approx 2\pi \cdot 0.0075/z^3$ (orange curve) and another fit $\sim 1/z^4$ (black curve). At larger sample linear sizes the weight of the propagating states increases and it is attractive, while the role of the plasma states decreases, so that derivative of E_{tot}^n , the Casimir force, decreases. In Fig. 7 we plot E_{tot}^n , per unit

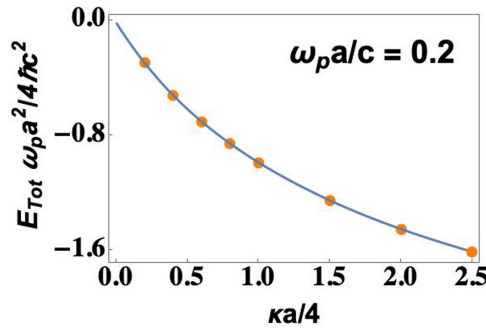


FIG. 7. Total energy E_{tot}^n per unit surface from Eq. (28), at various potential strengths κa for the linear width of the sample $ac/\omega_p = 0.2$. A constant prefactor has been adjusted to scale the amplitude of the result at values corresponding to Fig. 6, when $\kappa d = 0.005$.

surface, derived from the scattering model of Eq. (26) for the linear width of the sample $ac/\omega_p = 0.2$, at various potential strengths κa . A constant prefactor has been adjusted to scale the amplitude as in Fig. 6.

IV. THE TE MODE PROPAGATION IN THE SUPERCONDUCTING PHASE

A. Why photons should propagate in the superconducting phase, below the AH threshold

In the superconducting phase, the Anderson-Higgs (AH) mechanism makes the three EM modes massive, with mass $\hbar c m = 2\pi \hbar c / \lambda_L^\perp$, where λ_L is the London penetration length of the field components into the sample. Here c is the photon velocity in the medium. Propagation only occurs at energy $> \hbar c m$ with the dispersion $\omega_{\vec{k}}/c = \sqrt{m^2 + k_\perp^2 + k_\parallel^2}$. The two transverse massive modes are similar to the TM mode of the normal phase at the surfaces, but they decay in the interior of the material. They both couple to the MS surface excitation mode. In a macroscopic approach [i.e., based on a model for $\epsilon(\omega)$], the TE mode does not couple to surface plasma modes in the ideal normal metal film, at least within first-order perturbation theory. This is the reason why it is usually assumed that the TE photon contribution to the Casimir energy is quite scarce in the normal phase. In the superconducting phase, the longitudinal massive photon mode can be assimilated to a TE mode because of the nonvanishing B_z component. As $E_z = 0$, we are confident that no current is injected in the superconductor, a crucial requirement at low frequencies. However, being massive, the longitudinal mode should not propagate across the slab if it is relatively thick. Close to the transition temperature, the penetration length λ_L^\perp is quite long ($\sim 2.6 \mu\text{m}$ at $T \sim 86.5 \text{ K}$). Hence, we can expect that the length of the sample $a \lesssim \lambda_L^\perp$. Away from the transition temperature, the AH mass is rather large and states with energy above it are not expected to contribute much differently between the normal and superconducting phases. In fact, as in the case of the CG TM mode, the large enhancement of QP excitations in the density of states of the superconducting phase at the pair-breaking energy suggests that TE photon tunneling can be assisted by virtual excitations with QP's production in the a - b planes. Indeed, the pair-breaking energy is much lower

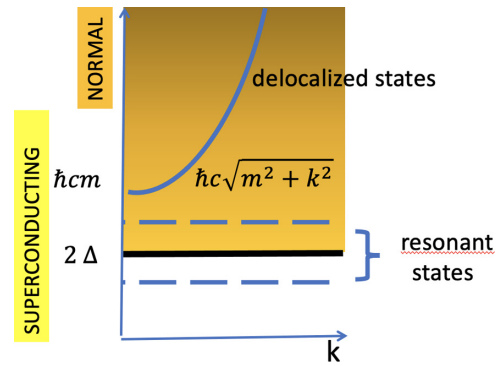


FIG. 8. Sketch of the energy dispersion versus k for $k_\parallel = 0$. Two resonant states are sketched below the band of delocalized states of the massive Anderson-Higgs modes, as they merge in the gapped energy window. c is the photon velocity in the medium and $m = 2\pi/\lambda_L^\perp$, where λ_L^\perp is the London penetration length in the c direction for YBCO. At high energy the linear dispersion of the normal phase is recovered.

than $\hbar c m$ in HTS (see Fig. 8). However, the question arises if the longitudinal mode takes advantage of photon resonances at energy below $2\Delta < \hbar c m$, to propagate across the sample. Resonances can be induced by virtual coupling with the in-plane superconductivity, originating from virtual excitations with broken pairs bound of the a - b planes. The answer is positive. The search for these resonances is the content of Secs. IV B and IV C. They characterize the superconducting phase and are expected to give an appreciable contribution to the Casimir energy difference.

As discussed in the Introduction, on the one hand we cannot account for the microscopic structure of the array of CuO planes in the lattice. The scale of k_\perp for photons interacting with the planes in the lattice is of the order of the inverse of the lattice spacing, which, in YBCO is $a \sim 3 \text{ nm}$. On the other hand, a photon in the micro infrared frequency range can only see a mediated structure of cells. We will adopt a scattering approach for a model structure and we will show that virtual pair-breaking processes in interaction with the photon field allows for resonant longitudinal states in the AH gap. The TE photon modes are well defined and long lived as long as they are located in energy below the 2Δ threshold and contribute to the Casimir energy. In our model we assume no space dependence in the a - b plane, for simplicity, which corresponds to $k_\parallel = 0$ and we will drop the label \perp in the following.

We now describe the model interaction in some detail. We assume a bulk high- T_c material with planar boundary surfaces and consider scattering in the \hat{z} direction, orthogonal to the surface, with \hat{z} parallel to the c axis for simplicity. This implies that the surfaces exposed to the impinging radiation are flat a - b (CuO) planes. The vacuum radiation of energy $\hbar\omega_{\vec{k}}/2$ is characterized by a component of the wave vector k orthogonal to the planes and a transverse component k_\parallel , parallel to the planes. A TE photon of infrared frequency, with a wave-vector component k_\parallel in the surface plane, can break a number N of pairs. N is of the order of 10^4 – 10^6 for microwave photons. However, as the film is macroscopic and superconducting, it does not conserve the pair number anyhow. Let $\epsilon = -\Delta$ be

the binding energy of a pair. We consider as ground state (GS) of the system the state of the superconducting plane of energy $N\epsilon$ in which N pairs are unbroken [24] and there is no real photon and we denote it by $|0, \uparrow\rangle$. On the other hand, $|1, \downarrow\rangle$ is the excited state in which N pairs are broken and a real photon is present, trapped in the film. Let us assume that a potential matrix element Ω couples these two states and the Hamiltonian applied to these states, with $k_{\parallel} \sim 0$, reads as

$$\begin{aligned} H_N \begin{pmatrix} |1, \downarrow\rangle \\ |0, \uparrow\rangle \end{pmatrix} &= \begin{pmatrix} -N\epsilon + \hbar\omega_k & \Omega \\ \Omega & N\epsilon \end{pmatrix} \begin{pmatrix} |1, \downarrow\rangle \\ |0, \uparrow\rangle \end{pmatrix} \\ &= \left[\frac{\hbar\omega_k}{2} + \frac{1}{2} \begin{pmatrix} -2N\epsilon + \hbar\omega_k & \Omega \\ \Omega & 2N\epsilon - \hbar\omega_k \end{pmatrix} \right] \\ &\quad \times \begin{pmatrix} |1, \downarrow\rangle \\ |0, \uparrow\rangle \end{pmatrix}. \end{aligned} \quad (29)$$

The eigenvalues are $\mathcal{E}_{\pm} = \frac{\hbar\omega_k}{2} \pm \frac{1}{2}\sqrt{\delta^2 + \Omega^2}$, with $\delta = 2N\epsilon - \hbar\omega_k$:

$$\begin{aligned} \mathcal{E}_- &\approx \frac{\hbar\omega_k}{2} - \frac{1}{2}|\delta|\sqrt{1 + \frac{\Omega^2}{\delta^2}} = +N\epsilon - \frac{1}{4}\frac{\Omega^2}{|\delta|}, \\ \mathcal{E}_+ &\approx \frac{\hbar\omega_k}{2} + \frac{1}{2}|\delta|\sqrt{1 + \frac{\Omega^2}{\delta^2}} = \hbar\omega_k - N\epsilon + \frac{1}{4}\frac{\Omega^2}{|\delta|}. \end{aligned}$$

The state corresponding to \mathcal{E}_- is

$$|-\rangle = \cos\theta |0, \uparrow\rangle + \sin\theta |1, \downarrow\rangle \quad (30)$$

with θ close 1 and is the GS of the system, while the excited state corresponding to energy \mathcal{E}_+ is

$$|+\rangle = -\sin\theta |0, \uparrow\rangle + \cos\theta |1, \downarrow\rangle. \quad (31)$$

Higher excited states are disregarded.

In a scattering approach, the interaction is localized in the film, while the incoming photon and the superconductor, very far from the scattering area and in the vacuum, are in the uncoupled state $|\Psi_0\rangle = |0\rangle|\uparrow\rangle$. The pair number is not conserved, so that we can assume that the energy \mathcal{E}_- is equal to the energy of the state $|\Psi_0\rangle$, in which the incoming photon and the superconductor are uncoupled, neglecting second-order contributions to the energy in the coupling Ω . We discuss the zero-temperature case and the channel of energy \mathcal{E}_+ is closed.

B. Scattering approach to the longitudinal mode propagation

We first discuss the scattering of a virtual photon from the vacuum into the AH modes inside the superconductor, at energy above the AH mass threshold $\hbar cm$. Being the AH modes longitudinal, it can be matched with the TE mode impinging on the superconductor surface. The wave function of the photon of wave vector \vec{k} is delocalized everywhere in the space at the left-hand (L) side of the metal chunk and it is scattered and transmitted to the right-hand (R) side of it. To characterize the scattering of a photon on the superconductor, at least in the limit of $k_{\parallel} \rightarrow 0$, the simplest scattering approach will be adopted, with two δ potentials at distance $2d$ to mimic the matter-radiation model interaction at the two planar surfaces of the superconducting film (see Fig. 9). To keep some analogy between the scattering approach and the original geometry, we have to include also the very left space

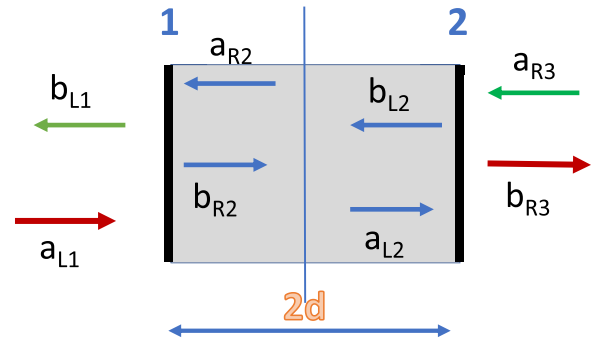


FIG. 9. Sketch of the model film (gray zone) with two δ functions (black thick lines at the boundaries) at a distance $2d$. a amplitudes refer to incoming channels, while b amplitudes refer to outgoing channels.

region and very right side one, as in Fig. 9. The total length of the scattering region, symmetric with respect to the origin, is $a = 4d$.

To show how the boundary conditions for the electric field are set at the film surface, we first consider just one planar surface interaction at $z = 0$ in free space. The “incoming” state is $|\Psi_0\rangle = |0\rangle|\uparrow\rangle$. We denote just by k the component k_z orthogonal to the surface plane and we make explicit the label for the parallel component of the k vector k_{\parallel} . The wave functions $\psi_{L,R}$, defined outside the scattering region at $z = 0$, are

$$\begin{aligned} \psi_L &= e^{ikz} |0, k_{\parallel}\rangle + r e^{-ikz} |0, k_{\parallel}\rangle + s e^{\kappa_L z} |1, k_{\parallel}\rangle, \\ \psi_R &= t e^{ikz} |0, k_{\parallel}\rangle + \tau e^{-\kappa_R z} |1, k_{\parallel}\rangle. \end{aligned} \quad (32)$$

r and s (t and τ) are reflection (transmission) amplitudes for the two channels of transverse wave vector k_{\parallel} . $|0, k_{\parallel}\rangle$ and $|1, k_{\parallel}\rangle$ are photon states. The channel $|1, k_{\parallel}\rangle$ is assumed to be closed, so that $\kappa_{L/R}$ are real parameters depending on the incoming energy and on k_{\parallel} , which is assumed to be conserved.

The superposition of the states Ψ_0 , with Ψ , defined above, due to the interaction, provides the field wave function at fixed k_{\parallel} , as a function of energy and k orthogonal to the plane. In the case of the δ -function potential, the matching conditions require continuity of the wave function at the scattering plane, $z = 0$, and a jump of the space derivative there:

$$|\psi_L(z=0)\rangle = [|\chi_- \rangle + \beta|+\rangle]_{z=0} = |\psi_R(z=0)\rangle, \quad (33)$$

$$\left. \frac{d|\psi_L\rangle}{dz} \right|_{z=0^-} - \left. \frac{d|\psi_R\rangle}{dz} \right|_{z=0^+} = gV \{|\chi_- \rangle + \beta|+\rangle\}_{z=0}, \quad (34)$$

where $|\chi_- \rangle = |\Psi_0\rangle + \alpha|-\rangle$ [$|\pm\rangle$ have been defined in Eqs. (30) and (31) and we assume $|\Psi_0\rangle$ and $|-\rangle$ to have the same energy] and α, β are complex numbers.

Tracing away the state of the condensate in the plane, Eqs. (33) and (34) should be projected onto $|0, k_{\parallel}\rangle[|\uparrow\rangle + |\downarrow\rangle]$ and $|1, k_{\parallel}\rangle[|\uparrow\rangle + |\downarrow\rangle]$ to derive the dependence of α, β on κ_L, κ_R, k as reported in Appendix B.

At maximum superposition, $-\sin\theta = \cos\theta = \frac{1}{\sqrt{2}}$, is

$$\alpha + \beta = \frac{gV}{2\kappa_+} \left[1 + \frac{\kappa_+}{2ik} \right],$$

$$\alpha - \beta = \frac{gV}{2\kappa_+} \left[1 - \frac{\kappa_+}{2ik} \right] \quad (35)$$

($\kappa_+ = \kappa_L + \kappa_R$). Unitarity of the S matrix fixes the ratio $\frac{gV}{2\kappa_+}$:

$$\frac{gV}{2\kappa_+} = -i \frac{\kappa_+}{2k} \frac{1}{1 + \left(\frac{\kappa_+}{2|k|}\right)^2}. \quad (36)$$

By taking the inverse decay length corresponding to the Meissner effect in the superconductor $\kappa_+/2 = m$ all parameters are fixed, except a mixing angle η , so that the S matrix for one single δ barrier is ($x = \frac{\kappa_+}{2k}$)

$$S = \begin{pmatrix} r & 0 & t & 0 \\ 0 & s & 0 & \tau \\ t & 0 & r' & 0 \\ 0 & \tau & 0 & s' \end{pmatrix} = \begin{pmatrix} -\frac{ixu}{1+ix} & 0 & \frac{\sqrt{1+x^2v^2}}{1+ix} & 0 \\ 0 & -\frac{ixv}{1-ix} & 0 & \frac{\sqrt{1+x^2u^2}}{1-ix} \\ \frac{\sqrt{1+x^2v^2}}{1+ix} & 0 & -\frac{ixu}{1+ix} & 0 \\ 0 & \frac{\sqrt{1+x^2u^2}}{1-ix} & 0 & -\frac{ixv}{1-ix} \end{pmatrix}, \quad (37)$$

where $u = \cos \eta$ and $v = \sin \eta$. We have excluded direct interaction between channels $|0, k_{\parallel}\rangle$ and $|1, k_{\parallel}\rangle$. Such an interaction would give an output amplitude in the $|1, k_{\parallel}\rangle$ channel, which is an inelastic process, which would lead to dissipation. At $\theta = -\pi/4$ in Eqs. (30) and (31), the parameter η does not play any role because, being the channels independent, every dependence on η is washed out by unitarity. The restriction $t' = t$ adopted here is allowed in the search of bound states provided time reversal holds. Equation (37) extends the S matrix for elastic scattering with one single channel;

$$\begin{pmatrix} b_L \\ b_R \end{pmatrix} = \begin{pmatrix} r & t' \\ t & r' \end{pmatrix} \begin{pmatrix} a_L \\ a_R \end{pmatrix}. \quad (38)$$

The wave-function amplitudes $a_{L/R}$ are the *in*-wave-function amplitudes, while $b_{L/R}$ are the *out*-wave-function amplitudes for the AH mode. In our case, each element is a 2×2 matrix because it includes the channel label 0,1, corresponding to photon states $|0, k\rangle$ and $|1, k\rangle$.

Now we turn to the geometry of Fig. 9 by using the following procedure [25,26]. The S matrices $S_{1,2}$ of each of the δ functions are translated by $\pm d$, respectively, with respect to the origin, by means of a unitary matrix $\Lambda(\pm d) = \text{diag}[e^{\pm ikd}, e^{\pm ikd}]$, where k is the k vector corresponding to the energy of the incoming photon. Next, the transfer matrices corresponding to $S_{1,2}$ are derived, defined as

$$\begin{pmatrix} b_{Ri+1} \\ a_{Ri+1} \end{pmatrix} = M_i \begin{pmatrix} a_{Li} \\ b_{Li} \end{pmatrix}.$$

The chaining $M_2 * M_1$ corresponding to matrix multiplication provides

$$\begin{pmatrix} b_{R3} \\ a_{R3} \end{pmatrix} = M_2 M_1 \begin{pmatrix} a_{L1} \\ b_{L1} \end{pmatrix}.$$

The final step is to transform back the full transfer matrix to give the global scattering matrix S' ,

$$\begin{pmatrix} b_{L1} \\ b_{R3} \end{pmatrix} = S' \begin{pmatrix} a_{L1} \\ a_{R3} \end{pmatrix}, \quad (39)$$

with the result

$$S' \equiv \begin{pmatrix} e^{-ika} s_{11} & e^{-2ik(a+d)} U_{\delta} s_{12} \\ e^{2ikd} s_{21} & e^{-ika} U_{\delta} s_{22} \end{pmatrix} \equiv \begin{pmatrix} S_{11} & S_{12} \\ S_{21} & S_{22} \end{pmatrix}$$

where

$$s_{11} = r_1 + t'_1(1 - t_2 r'_1)^{-1} t_2 t_1,$$

$$s_{12} = t'_1(1 - t_2 r'_1)^{-1} r'_2 e^{-2ikd},$$

$$s_{21} = e^{2ikd} r_2 [1 - r'_1 t_2]^{-1} t_1,$$

$$s_{22} = t'_2 + e^{2ikd} r_2 r'_1 (1 - t_2 r'_1)^{-1} r'_2 e^{-2ikd},$$

$$U_{\delta} = e^{2ikd} e^{2ik(a+d)} s_{11} s_{22}^{-1\dagger} s_{12}^{\dagger} s_{21}^{-1} \equiv e^{2ika} \begin{pmatrix} e^{2i\delta_1} & 0 \\ 0 & e^{2i\delta_2} \end{pmatrix}. \quad (40)$$

r_i and t_i are the 2×2 matrices defined in Eq. (37). Translation by $\Lambda(\pm d)$ implies that the matrices r_2, r'_2 acquire a phase $e^{\pm 2ikd}$ with respect to r_1, r'_1 . $\delta_{1,2}$ are the phase shifts of the two channels within the cell due to the scattering. This is the result of Guérout *et al.* [26]. Note a small difference in the ordering in S'_{11} . Numerically, our scattering matrix is found to be unitary.

The S matrix is numerically found to be unitary. Besides, as can be checked numerically:

$$S_{11} S_{22}^{-1\dagger} S_{12}^{\dagger} S_{12}^{-1} = 1 \quad \text{and} \quad S_{12} = -S_{21}. \quad (41)$$

From the definitions of S_{ij} and s_{ij} and the last equality we get

$$U_{\delta} \equiv -e^{4ikd} s_{21} s_{12}^{-1}. \quad (42)$$

Note that, in the case of elastic scattering with a single channel, if we put

$$S' = \begin{pmatrix} r & t^* e^{-2i\delta} \\ t & -r^* e^{-2i\delta} \end{pmatrix}, \quad (43)$$

the condition $S_{11} S_{22}^{-1\dagger} S_{12}^{\dagger} S_{12}^{-1} = 1$ provides $r(-r^{-1} e^{-2i\delta}) t e^{2i\delta} t^{*-1} e^{2i\delta} = 1$, that is, $e^{-2i\delta} = -t/t^*$, as expected.

C. TE resonant contribution to the Casimir energy for the superconducting phase

In the case of the superconducting phase, extended propagating states below the Meissner AH threshold are not allowed. However, analysis of the S matrix of Eqs. (39) and (40) shows that there can be one or more resonant states propagating across the superconductor, below the Meissner threshold, as sketched in Fig. 8. Their signatures are the zeros of the determinant $\text{Det}\{S'[k] - 1\}$. In Fig. 10 we report a plot of the real and imaginary parts of the determinant. The zeros appear at energies $k_1 \equiv \omega_{k_1}/(\hbar cm) = 0.2$ and $\bar{k}_2 = 0.9$ (in dimensionless unities), for a length of the sample $a = 0.378\lambda_L$. Here $k_{\parallel} = 0$ (normal incidence), for simplicity. Figure 11

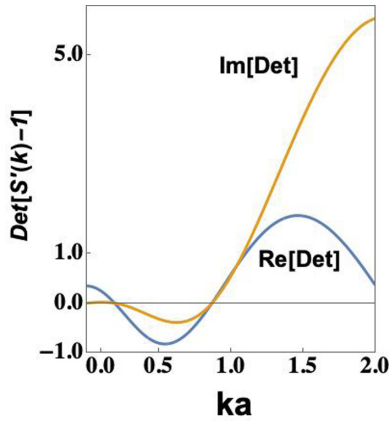


FIG. 10. Real and imaginary parts of the $\text{Det}\{S'[\bar{k}] - \mathbf{1}\}$ vs $\bar{k} = k/m$ for $a = 0.378\lambda_L$ and $k_{\parallel} = 0$. In these units the AH threshold is marked by $\bar{k} = 1$. Two resonant modes at low energy correspond to the zeros of $\text{Det}\{S'[\bar{k}] - \mathbf{1}\}$.

shows the energy trend of these two states with increasing length of the sample. The horizontal black line is the AH threshold and the propagation modes are fully delocalized above this energy. The green dashed line marks energy 2Δ , one tenth of $\hbar cm$ (the y axis is not in scale). In the energy interval $(2\Delta, \hbar cm)$ single QP's are produced by pair breaking and the modes acquire a finite lifetime. When the two modes are in the energy window $< 2\Delta$ in which a continuum of propagating modes is forbidden, they act as resonances in the propagation of the field. For $a < \lambda_L$, which corresponds to full penetration of the radiation inside the superconductor, the blue curve resonant mode is even with respect to the inversion center of the sample and is lower in energy. However, sustaining radiation inside the superconductor costs much energy when $a \approx \lambda_L$ and the even mode increases sharply by a very short lifetime (only the real part of the energy appears in the plot). For $a > \lambda_L$ the odd mode (red curve) becomes lower

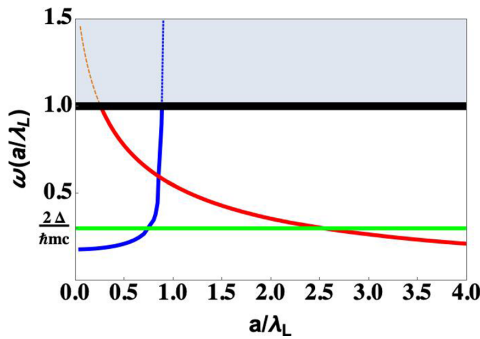


FIG. 11. Energy ω of the resonant longitudinal states (normal incidence), below the massive Anderson-Higgs propagating modes (gray area above the black horizontal line) inside the superconductor versus a/λ_L . $a = 4d$ is the length of the model sample in the direction orthogonal to the CuO planes. Energy, in the limit $k_{\parallel} = 0$, is in units $\hbar cm$, where c is photon velocity in the medium and $m = 2\pi/\lambda_L$. The red curve is the mode odd for $L \leftrightarrow R$ inversion, while the blue curve is even and has low energy only for $a < \lambda_L$. The green dashed line marks the threshold for pair-breaking excitations, at 2Δ . The vertical axis is not in scale.

in energy because it allows for small field amplitude with a node inside the superconductor. We renounce to qualify the field amplitude within the sample but we infer the parity of the modes from the parity of the phase shift across the sample when $k \leftrightarrow -k$. We expect that non-normal incidence ($k_{\parallel} \neq 0$) would mix the two modes particularly at intermediate lengths $a \sim \lambda_L^{\perp}$, by opening a gap at the crossing of the curves.

V. TOTAL CASIMIR ENERGY AND ENERGY DIFFERENCE

The total Casimir energy in the normal phase has been discussed in Sec. III C. Here we present our estimate for the total Casimir energy in the superconducting phase and the difference between the two.

A. Total Casimir energy in the superconducting phase

The total Casimir energy in the superconducting phase does not include propagating states below the Meissner AH threshold $\hbar cm$, except for the TE resonances. In our estimate we assume that the contribution coming from energies above the Meissner threshold and from the QP's in the energy window $(2\Delta, \hbar cm)$ is roughly canceled by a corresponding contribution in the normal phase, when we eventually take the difference. In fact, single QP delocalized states are present both in the superconducting and in the normal phases. The contribution to the total Casimir energy difference due to the marked change in the density of states close to the 2Δ threshold, between the two phases, is discussed in Appendix C. The 2Δ gap threshold induces a sizable change of the dielectric function, as discussed in Sec. II with important changes in the photon propagation at that energy range. However, if we are at temperatures rather away from T_c , we can expect that the weight of this contribution is scarce for microwave photons and we will ignore it. It is considered to be small and is neglected. There are no propagating states at energy below the gap threshold 2Δ , so that the only contributions to the Casimir energy which we consider for the superconducting phase arise from the TM plasma mode and the TE resonance (just one at the chosen lengths of the sample).

The symmetric TM mode, even with respect to $L \leftrightarrow R$ inversion symmetry, appears in Fig. 5. It is linearly dispersed in k_{\parallel} at small k_{\parallel} values, while it is dispersed as $\sqrt{k_{\parallel}}$ at larger k_{\parallel} . We follow the same steps as in Eq. (13) to subtract the $a \rightarrow \infty$ term and leave just the a -dependent contribution. Using Eq. (21) and cutting the $k_{\parallel}a/2 = s$ integration at $\bar{s} = 2\Delta\sqrt{2\epsilon_s}/\omega_0$, the contribution to the Casimir energy of the TM mode is approximately

$$E_{\text{Sup}}^{\text{TM}} = \frac{1}{2} \sum_{k_{\parallel}} \omega_{k_{\parallel}} = -\frac{1}{2} \left(\frac{2L}{2\pi a} \right)^2 2\pi \int_0^{\bar{s}} \frac{s^2}{2} ds \frac{\partial \omega(s)}{\partial s} \\ \approx -\left(\frac{2L}{a} \right)^2 \frac{\omega_0}{2\pi} 0.037, \quad (44)$$

in analogy with Eq. (13). Here $\omega_0 \lesssim 2\Delta$. Based on the fact that the MS mode has a $\sqrt{k_{\parallel}}$ dependence on k_{\parallel} , we estimate the integral in Eq. (44) by assuming $\omega_{ps} \sim \omega_p$ and $\omega_0 \sim 2\Delta/2\pi$. The result is plotted in Fig. 13 (blue curve).

The piling up of QP excitations near the gap threshold allows for an odd mode (which is the ‘‘neutral’’ ASPM) at those

energies but only at larger k_{\parallel} vectors [22]. Their influence is detected, according to our model, in the resonances that a TE photon propagating mode can encounter at low energy according to Fig. 11. This feature is absent in the normal metal phase. The contribution of the TE mode to the Casimir energy is negative for $\lambda_L^{\perp} > a$, i.e., when the working temperature is not far from T_c . Here we give an estimate of the TE resonance for $a = 0.378\lambda_L^{\perp}$ (see Fig. 10 and Sec. IV C). The energy of the resonance disappears for $a \rightarrow \infty$, so that we do not have to subtract any a -independent limiting contribution. The energy of the resonance is given by the zero of the determinant $\text{Det}\{S'[\vec{k}] - \mathbf{1}\}$ [with S' given by Eq. (40)] and takes the value $0.2\hbar cm$ when $k_{\parallel} = 0$. However, its k_{\parallel} dependence is weak, except for the fact that direct tunneling across the resonance does not contribute to the Casimir energy. Therefore, we add an angular dependence $(1 - \cos\theta)$ in the integration over k_{\parallel} and approximate the contribution as follows, with $s = \frac{k_{\parallel}a}{2} \in (0, s^{\max})$, where $s^{\max} \sim \frac{2\Delta}{\omega_0} \sqrt{\frac{\epsilon_s}{\pi}}$:

$$\begin{aligned} E_{\text{Sup}}^{\text{TE}} &\approx -\frac{1}{2} \left(\frac{2L}{2\pi a} \right)^2 0.2 \hbar cm \int_{-\frac{\pi}{2}}^{\frac{\pi}{2}} d\theta (1 - \cos\theta) \int_0^{s^{\max}} s ds \\ &= -\frac{1}{2} \left(\frac{2L}{2\pi a} \right)^2 0.2 \hbar cm \left(\frac{\pi}{2} - 1 \right) \left(\frac{2\Delta}{\omega_0} \sqrt{\frac{\epsilon_s}{\pi}} \right)^4 \quad (45) \end{aligned}$$

The dispersion in energy vs linear size of the sample appears in Fig. 13 (orange curve). Its weight in the density of states is rather small and this implies that it gives a little contribution to the Casimir energy. In particular, the contribution changes sign at $\lambda_L^{\perp} \sim a$ (see Fig. 11), but it is anyhow vanishingly small for $a > \lambda_L^{\perp}$.

In our model, the TE resonances arise from bound states that are split off the delocalized AH band with threshold $\hbar cmk = 1$ in our units. In the superconducting phase there is a continuum of electronic QP states of energy above the pair-breaking threshold energy 2Δ . They could contribute to the transfer of photons across the sample, so that we can assume that there is a continuum of photonic states corresponding to their energy. We comment on these delocalized photonic states here in the following. Our model system acts as a 1D potential well of length a which can bound states. As a function of energy ω the change of the density of states due to the scattering, derived from the Green's functions defined by $G = G_0 + G_0 t G_0$ (t is the t matrix defined in Appendix A), is given by

$$\begin{aligned} \Delta\nu(\omega) &= -\frac{1}{\pi} \text{Im Tr}\{G^R - G_0^R\} \\ &= \frac{1}{2\pi i} \frac{d}{d\omega} \ln \text{Det } S'(\omega) \quad (46) \end{aligned}$$

(the label R denotes ‘‘retarded Green’s function’’). As $|\text{Det } S'(\omega)| = 1$, $\Delta\nu(\omega) = \frac{1}{\pi} \sum_j \frac{d}{d\omega} \delta_j(\omega)$, where δ_j are the phase shifts of the two channels ($j = 1, 2$).

The matrix S' can be set in a block form, diagonal in the channel label j . The contributions of Eq. (46) coming from the phase shifts $\delta_{1,2}$ should be included in our estimate of the Casimir energy for the longitudinal mode and compared with the corresponding ones of the TE mode of the normal phase. In particular, channel 1 would refer to processes which occur

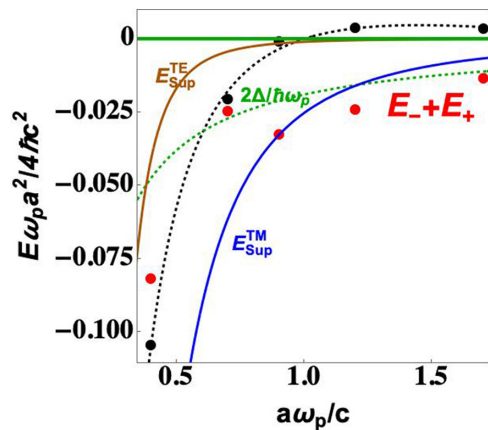


FIG. 12. Various contributions to the Casimir energy difference (per unit surface) vs linear size of the sample. The red dots are the contribution given by the plasma excitations in the normal phase (from Fig. 6), labeled as $(E_+ + E_-)$. $E_{\text{Sup}}^{\text{TM}}$ is the TM plasma mode in the superconducting phase [blue curve, from Eq. (44)]. $E_{\text{Sup}}^{\text{TE}}$ is the TE plasma mode in the superconducting phase induced by coupling with pair-breaking processes [orange curve, from Eq. (45)]. The difference $\delta\mathcal{E} = E_{\text{Sup}}^{\text{TM}} + E_{\text{Sup}}^{\text{TE}} - (E_+ + E_-)$ is marked by the black dots (the dashed black curve is a guide to the eye). The difference $\Delta\mathcal{E}$ becomes positive at larger sizes but vanishes for size going to infinity. The threshold for pair-breaking processes at various sizes is marked by the dashed green curve.

both in the normal metal phase and in the superconducting phase. As for channel 2, according to our model, its influence is only limited to the superconducting phase and mimics processes in which propagation includes Cooper pair-breaking events, close to energy 2Δ . A similar contribution was presented in the macroscopic approach for the TM modes in Sec. III B. We argued there that pair-breaking processes make the largest difference, but can be assumed to have little role at our much lower incoming photon energies, except for virtual excitation. We are not including these contributions that had been already discarded in the case of the TM modes.

In Fig. 13 we have plotted the derivative of the phase shift $d\delta_2/dk$ vs energy k (in dimensionless units) for various lengths of the sample in units of λ_L^{\perp} . A sharp drop for $k \lesssim 1$ in the curve for $a \lesssim 1.6$ marks the splitting of a bound state related to channel 2 from the bottom of the AH energy dispersion. The bound state appears as a π jump in the phase shift $\delta_2(k)$. Bound states appear as π jumps in both channels, as shown in the inset of Fig. 13, where the phase shifts $\delta_{1,2}$ are plotted vs k , for $a = 2.55$. In fact, the potential formed by the two δ functions acts as an attractive potential well for the photons. It follows that bound states are split from the bottom of the AH energy dispersion and move to lower energy with increasing distance between the δ peaks. At given coupling strength, the threshold thickness of the sample for the appearance of a bound state splitted off channel 2 is $a \lesssim 1.6$.

B. Casimir energy difference $\delta\mathcal{E} = E_{\text{Sup}} - E_{\text{Nor}}$

Figure 12 summarizes our estimates of the contributions to the Casimir energy per unit area for a sample of linear size a . The black dots are evaluations of the energy difference

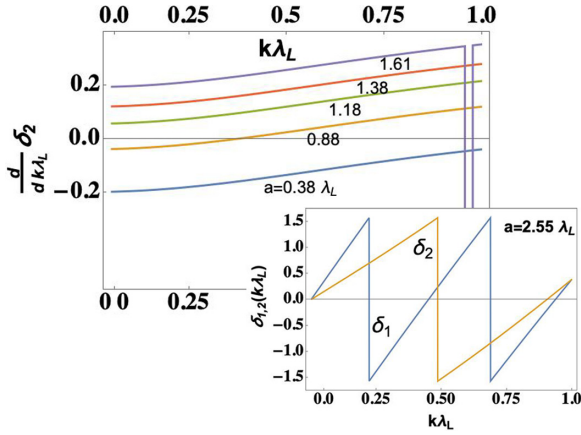


FIG. 13. Derivative of the phase shift $d\delta_2/dk$ vs energy k (in dimensionless units) for $a = 0.38, 0.88, 1.18, 1.38, 1.61$ (from bottom to top). At $a \approx 1.6$ a bound state splits off the bottom of channel 2, $k = 1$ and the contribute with a δ -like peak to the derivative (exaggerated in the picture). Inset: Phase shift δ_1 (blue) and δ_2 (orange) for $a = 2.55$. The π jumps in $\delta_{1,2}$ mark two bound states in channel 1 and one bound state in channel 2.

$\delta\mathcal{E} = E_{\text{Sup}} - E_{\text{Nor}} = E_{\text{Sup}}^{\text{TM}} + E_{\text{Sup}}^{\text{TE}} - (E_+ + E_-)$ between the superconducting and the normal phases of the sample, at few a values. In our estimate only the contributions coming from the plasma excitations are included. In Sec. III C, we have qualitatively estimated the contribution coming from the delocalized photonic states in the normal phase as $E_{\text{tot}}^n - (E_+ + E_-)$, but we have not included them. In the energy range $\omega > 2\Delta$ they are also present in the superconducting phase (although with a slightly different density of states except for energies in proximity of 2Δ) because photonic transmission can be assisted by the delocalized electronic QP states at these energies and we can surmise that these terms contribute roughly equally in the two phases. However, we have also neglected this contribution for energies $\omega < 2\Delta$, which is present for the normal phase only because, as it appears in Fig. 6, the energy difference $E_{\text{tot}}^n - (E_+ + E_-)$ is rather small not only at small sample sizes, but even at larger sample sizes [we have plotted also 2Δ in Fig. 6 (green dashed line), which is devoted to the normal phase, for reference]. Besides, E_{tot}^n was estimated by means of the scattering model of Sec. III C and has been adapted, but is not homogeneous with the rest of the calculation. The brute approximation of neglecting $E_{\text{tot}}^n - (E_+ + E_-)$ altogether implies that larger linear sizes of the sample are not displayed in Fig. 12. At those sizes, the two δ potentials develop bound states also in channel 1, as shown in the inset of Fig. 13 and the scattering model becomes unreliable.

Inspection of the location of the black dots in Fig. 12 vs linear size of the sample [$(a\omega_p/c, \delta\mathcal{E}) \approx (0.4, -0.1), (0.7, -0.02), (0.9, 0), (1.2, 4 \times 10^{-3}), (1.7, 3 \times 10^{-3})$] shows that the gain in Casimir energy $\delta\mathcal{E}$ when the sample undergoes the phase transition sharply depends on the linear size of the sample and can even become a loss when the size increases. This can be justified by noting that, in the normal phase, the absolute number of electronic QP states increases with the size, with an increase of the $|E_{\text{tot}}^n|$ magnitude, while the 2Δ gap in the superconducting phase reduces chances

for photon transmissions assisted by QP's and, hence, for contributions to Casimir energy gain.

A tradeoff between temperature and linear size of the sample is also strictly required. On the one hand, a temperature $T \ll T_c$ implies that $\omega_{ps} \sim \omega_p$ because the density of pairs exhausts the full electron density, and $\delta\mathcal{E}$ would increase. But, in the London theory, $c/\omega_{ps} \sim \lambda_L^\perp$ and a shorter λ_L^\perp (for $T \ll T_c$) implies that we move to larger $a\omega_p/c$ values with a sharp reduction of $\delta\mathcal{E}$. On the other hand, a temperature closer to T_c would increase λ_L^\perp and move to lower values of $a\omega_p/c$ of Fig. 12, thus increasing the gain in Casimir energy $\delta\mathcal{E}$, but ω_{ps} would become much smaller than ω_p and the magnitude of $\delta\mathcal{E}$ is reduced. Besides, fluctuations would dramatically increase, especially in a HTS, with a destructive role. In our derivation we have been choosing $\omega_{ps} \sim \omega_p$.

Assuming a cubic sample, so that $L = c/\omega_p = a$ and by choosing a reference value for $\hbar\omega_{ps} \sim \hbar\omega_p \approx 40$ meV we get $\delta\mathcal{E} \sim -1.4 \times 10^{-5}$ eV. This is an optimistic reference energy scale, with more than an order of magnitude uncertainty. A better characterization of the result requires the choice for an appropriate temperature, which also depends on estimates of the refraction index of the sample in the normal and superconducting phase in the range of microwaves and of the plasma frequency in the two phases.

VI. SUMMARY AND CONCLUSION

The Archimede project is designed for measuring the effects of the gravitational field on a Casimir cavity by performing a weighing measurement of the vacuum fluctuation force on a rigid Casimir cavity [2–4]. This paper discusses the various contributions to the Casimir energy assuming that the “cavity” is just a metal bulk sample (a cube or slab) in vacuum. As a reference metal we take YBCO, which undergoes the superconducting phase transition at $T_c \sim 90$ K. The experiment will measure differences in weight between the superconducting and the normal phase by weighting at two different temperatures, above and below T_c .

A key point of the interpretation of the results of the experiment will be the estimate of the contribution of the Casimir energy to the total transition energy in the two phases and, correspondingly, to the weight variation.

It has been recently proposed that the Casimir energy is a big part of the “condensation energy” so that the driving mechanism for phase transition is the Casimir energy itself [6].

Up to now, the Casimir force has been measured in cavities of micron sizes [27] while the Casimir contribution to the transition energy for tens of nanometer cavities has been theoretically and experimentally investigated within a previous experiment [4,28–30], confirming that the expected energy range for density of state changes in the photon field due to the presence of the cavity corresponds to far infrared and microwaves. At least in conventional superconductors where electron-phonon coupling is considered as the pairing mechanism, the lattice parameter is the scale at which forces related to condensation energy act. Photons with a wavelength comparable to the lattice parameter have huge energy and it is reasonable to expect that they propagate across the cavity with no harm whatsoever.

In this work we limit ourselves to an estimate of the Casimir energy change by comparing the zero-point energy of the superconducting and the normal phases in a macroscopic sample. There are various contributions to the zero-point energy of the photon field. Let us enumerate these contributions, starting from the normal phase and continuing with the superconducting phase, afterwards.

In the normal phase one contribution arises from the continuum of TM modes propagating across the sample in case the skin depth δ of the E_z penetrating field is comparable with the linear size of the metal slab (in direction z), while the continuum of TE modes should not contribute, except for tiny surface magnetization effects, due to the reduced penetration of B_z , in the case of a paramagnetic material. Of course, propagation can be assisted by the continuum of electronic QP excitations in the sample via nonelastic processes. The TM polarization contributes with plasma modes (charge excitations) localized at the surface in the normal phase. There are two plasma surface modes for the sample with two surfaces. In case of a $z \leftrightarrow -z$ inversion-symmetric sample, they are a symmetric mode (SPM) and an antisymmetric plasma mode (ASPM). They are derived in a macroscopic approach using the Drude formula for the dielectric function which is valid in the limit of large inelastic scattering time $\tau \rightarrow \infty$ and are discussed in Sec. II and denoted as E_{\pm} . We stress that retardation is important to obtain the correct dispersion for small k vectors, k_{\parallel} (parallel to the surfaces of the sample, assumed to be planar). The energy scale which characterizes the plasma excitations, which couple to the photonic field, is the plasma frequency ω_p , or, better $\omega_p/\sqrt{2}$ (see Fig. 3).

The contribution due to the continuum of TE modes has been estimated by a simple analogical scattering model where the bulk material is reduced to a potential made of two δ -repulsive functions at distance $2d$ along the \hat{z} direction, which provide elastic transmission and reflection of the incoming wave. The linear thickness of the sample a has been related to a full size of $4d = a$. The model is presented in Sec. III C. As the model has only qualitative relevance, we did not even include difference in the propagation velocity between vacuum and material, for simplicity. The model is quite useful, though, because, when continued analytically to imaginary energies, it allows to get an estimate of the total Casimir energy E_{tot}^n , including the plasma modes [23]. At very small sizes a , the contribution given by the continuum of states to E_{tot}^n is expected to be minor and we have used the information coming from E_{tot}^n , by shifting the curve of the corresponding energy vs linear size a so to match $E_+ + E_-$ at small a . It turns out that the discrepancy between E_{tot}^n and $E_+ + E_-$ only occurs for large a values, in a range of a values which is not reliable for reasons that will be explained below. The model is part of a more general model which includes two channels to be described below, presented in Sec. IV. Analysis of the extended model shows that when the size a increases beyond $a > 1.5$, undesired resonant states are produced in the elastic channel (see Fig. 13 inset). This is the reason why the model should not be accepted at large a values.

Modelization of the superconducting phase requires three energy scales. The highest one in energy is the Anderson-Higgs threshold $\hbar cm$ (c is the propagation velocity in the medium and $m = 2\pi/\lambda_L^{\perp}$). Photons acquire the AH mass and

a longitudinal mode arises, eating up the phase mode of the superconducting order parameter. The intermediate one is the superconducting plasma frequency ω_{ps} and the lowest one is the Cooper pair-breaking threshold 2Δ . They are discussed in Sec. II. At energies below the AH threshold light does not propagate (radiation gap), unless it is coupled to quasiparticle (QP) excitations. The difference with the normal phase is substantial in the energy window defined by the electronic superconducting gap Δ . However, QP's can originate at finite temperature from nodes in the gap or any type of pair-breaking process. We do not consider the continuum of propagating photon states for energies above the 2Δ threshold because we have neglected the corresponding states in the normal phase and, except for marked changes in proximity of 2Δ , which are in any case dropped, we assume that this energy range of both spectra roughly cancels in the difference. The TM photon mode has $B_z = 0$ at the surfaces and satisfies the macroscopic London equation. This is the reason why we can keep a macroscopic picture when discussing the transverse massive EM fields at the surfaces, each of which roughly corresponds to the EM TM field of the normal phase. Both of them couple to the plasma excitations of the sample in the superconducting phase. There are two plasma modes in the superconducting phase of limited geometries, which can be derived in a hydrodynamic approach [22]: The Mooij and Schön (MS) acoustic mode and the Carlson-Goldman (CG) mode. The first one corresponds to the SPM of the normal phase and has a $\sqrt{k_{\parallel}}$ dispersion and lies within the superconducting gap (see Fig. 5). The CG mode is in proximity of the 2Δ threshold and involves QP's which neutralize the charge in a sort of ASPM. This mode, being neutral, does not couple with radiation and is ignored. In addition, resonances can appear in the radiation gap, even in the 2Δ gap, which split off the AH threshold by virtual interaction with the Cooper pair condensates of the $a - b$ planes (see Fig. 11). They provide resonances which make the longitudinal massive mode propagating in the superconducting gap. We have shown that this is possible by setting up the scattering model of Sec. IV, with an elastic channel and a closed channel. Of the two resonances, a symmetric and an antisymmetric one, only one is present at energy below 2Δ , depending on the linear size of the sample. The antisymmetric one is only at low energies, when the size of the sample is $a > 2\lambda_L^{\perp}$ (see Fig. 11).

With the mentioned approximations, an estimate of the Casimir energy difference between the two phases $\delta\mathcal{E} = E_{\text{Sup}} - E_{\text{Nor}} = E_{\text{Sup}}^{\text{TM}} + E_{\text{Sup}}^{\text{TE}} - (E_+ + E_-) \sim -10^{-5} - 10^{-6}$ eV is reported for a few linear sizes of the sample in Fig. 12 for a reference area a^2 , where length is in units of c/ω_p and is marked by the black dots in the figure. The dependence on the linear size of the sample is $\sim 1/a^4$, for large sizes, as found in the measurement of the Casimir-Polder force [27]. The pair-breaking threshold 2Δ is also reported for comparison and longer samples imply that the energy window in the superconducting gap shrinks. To achieve these estimates, quite different qualitative models have been invoked: A macroscopic model for the TM polarization, a scattering "microscopic" model for the TE polarization both in the form of one-channel elastic scattering and in the form of a two-channel scattering. As the models have little justification and the correspondence between them is

arbitrary, the results cannot be considered as quantitative. They are just an indication of the physics involved, which should be checked carefully in the course of the experiment. It is clear that the largest contributions to the difference $\delta\mathcal{E}$ arise from the superconducting gap window and from the energy window across the pair-breaking threshold for the TM polarization (see Fig. 2). The latter contribution has been qualitatively discussed in Appendix C, but has not been included in our estimate and requires further consideration. The reference linear size of the sample is $a \sim c/\omega_p$ which is $\sim \lambda_L^\perp$ if $\omega_p \sim \omega_{ps}$. This is the choice that has been done to simplify our estimates, but we stress that it is the crucial point in the design of the experiment. As discussed in Sec. V B, an appropriate tradeoff between temperature and linear size of the sample is required. $\omega_p \sim \omega_{ps}$ implies that the pair electron density n_s exhausts the total electron density n , but this only happens at very low temperatures $T \ll T_c$. At these temperatures the effective linear scales of the normal and superconducting phases, which are dictated by the penetration depth of the photon field, are of the same order, provided the sample is close to be an ideal metal ($\omega\tau \gg 1$). However, the small value of λ_L^\perp implies that the linear size of the sample should be small if the boundary surfaces of the sample are supposed to have Casimir interaction and a very homogeneous slab should be synthesized, which reduces the measured weight. One can envisage a layered structure, which is also being considered by the team involved in the experiment [11].

ACKNOWLEDGMENTS

We acknowledge useful discussions with P. Lucignano and R. Fazio. Work was financially supported by the joint project of the Istituto Nazionale di Fisica Nucleare, the University of Sassari, the Istituto Nazionale di Geofisica e Vulcanologia (INGV), University of Cagliari, and IGEA S.p.a (project

SAR-GRAV, funds FSC 2014-2020); by University of Sassari with ‘‘Fondo di Ateneo per la ricerca, 2019 and 2020,’’ and by University of Napoli, ‘‘Federico II,’’ with project ‘‘time crystal,’’ Grant No. E69C20000400005.

APPENDIX A: t MATRIX AND CHANGE IN THE DENSITY OF STATES

With $G = G_0 + G_0 t G_0$, we have

$$\begin{aligned} \Delta\nu(\omega) &= -\frac{1}{\pi} \text{Im} \text{Tr}\{G^R - G_0^R\} \\ &= -\frac{1}{\pi} \text{Im} \text{Tr}\{G_0^R t G_0^R\}, \end{aligned} \quad (\text{A1})$$

$$G_0^R = [\omega + i0^+ - H_0]^{-1}, \quad \frac{dG_0}{d\omega} = -G_0^2,$$

$$\text{Tr}\{G_0 t G_0\} = \text{Tr}\{G_0^2 t\} = \text{Tr}\left\{-\frac{dG_0}{d\omega} t\right\}.$$

As $t = V \sum_{n=0}^{\infty} (G_0^R V)^n$, we have

$$\begin{aligned} \text{Tr}\left\{-\frac{dG_0}{d\omega} t\right\} &= \text{Tr}\left\{-\frac{dG_0}{d\omega} V \sum_{n=0}^{\infty} [G_0 V]^n\right\} \\ &= \sum_{n=1}^{\infty} \text{Tr}\left\{-\frac{dG_0}{d\omega} V [G_0 V]^{n-1}\right\} \\ &= \sum_{n=1}^{\infty} \frac{1}{n} \text{Tr}\left\{-\frac{d}{d\omega} [G_0 V]^n\right\} \\ &= \frac{d}{d\omega} \text{Tr}\{\ln [1 - G_0^R V]\}. \end{aligned} \quad (\text{A2})$$

It follows that

$$\begin{aligned} -\text{Im} \text{Tr}\{\ln [1 - G_0^R V]\} &= -\frac{1}{2i} [\text{Tr}\{\ln [1 - G_0^R V] - \ln [1 - G_0^A V]\}] = \frac{1}{2i} [\text{Tr}\{\ln [(1 - G_0^A V) (1 - G_0^R V)^{-1}]\}], \\ (1 - G_0^A V) (1 - G_0^R V)^{-1} &= (1 - G_0^A V) (1 + G_0^R V + G_0^R V G_0^R V + \dots) \\ &= 1 - (G_0^A - G_0^R) - G_0^A V G_0^R V + G_0^R V G_0^R V + \dots \\ &= 1 - (G_0^A - G_0^R) [V + V G_0^R V + \dots] = 1 - (G_0^A - G_0^R) t, \end{aligned}$$

$$G_0^A - G_0^R = 2i \delta(\omega - H_0), \quad S(\omega) = 1 - 2\pi i \delta(\omega - H_0) t(\omega),$$

$$\begin{aligned} \Delta\nu(\omega) &= -\text{Im} \frac{d}{d\omega} \text{Tr}\{\ln [1 - G_0^R V]\} = \frac{1}{2\pi i} \frac{d}{d\omega} \text{Tr}\{\ln [1 - 2\pi i \delta(\omega - H_0) t(\omega)]\} \\ &= \frac{1}{2\pi i} \frac{d}{d\omega} \text{Tr}\{\ln S(\omega)\} = \frac{1}{2\pi i} \frac{d}{d\omega} \ln \text{Det} S(\omega) = \frac{1}{\pi} \sum_j \frac{d}{d\omega} \delta_j(\omega) \end{aligned} \quad (\text{A3})$$

as $S(\omega) = \text{diag}[e^{2i\delta_j(\omega)}]$.

APPENDIX B: DERIVATION OF THE S MATRIX FOR SCATTERING ACROSS ONE SUPERCONDUCTOR PLANE

Starting from Eqs. (38) and (32) and projecting Eqs. (33) and (34) onto our basis (we trace on the state of the

superconducting condensate), we get equations for α, β

$$\begin{aligned} \langle 0, K | \psi_L(0) \rangle &\rightarrow 1 + r = 1 + (\alpha + \beta) \cos \theta, \\ \langle 1, K | \psi_L(0) \rangle &\rightarrow s = (\alpha - \beta) \sin \theta, \end{aligned} \quad (\text{B1})$$

$$\begin{aligned}
\langle 0, K | \psi_R(0) \rangle &\rightarrow t = 1 + (\alpha + \beta) \cos \theta, \\
\langle 1, K | \psi_R(0) \rangle &\rightarrow \tau = (\alpha - \beta) \sin \theta, \\
|dev\rangle &= \left. \frac{d|\psi_L\rangle}{dz} \right|_{z=0^-} - \left. \frac{d|\psi_R\rangle}{dz} \right|_{z=0^+} \\
&= g [|\Phi\rangle V + |\Phi'\rangle V^*]
\end{aligned} \tag{B2}$$

$$\begin{aligned}
\langle 0, K | |dev\rangle &\rightarrow i k(1 - r - t) = g[V(1 + \alpha) + V^*\beta] \cos \theta \\
\langle 1, K | |dev\rangle &\rightarrow \kappa_L s + \kappa_R \tau = g[V\alpha - V^*\beta] \sin \theta,
\end{aligned} \tag{B3}$$

where $|\Phi\rangle$ and $|\Phi'\rangle$ are defined in Eqs. (30) and (31). Here we observe that the structure reflects the usual δ -function potential in a one-dimensional Schrödinger equation. Continuity of wave function and jump in the derivative provide ($g > 0 \rightarrow$ repulsive δ barrier in the following)

$$\begin{aligned}
1 + r &= t, \quad ik(1 - r) - ikt = -gt, \\
1 + r &= t, \quad 1 - r = \left(1 - \frac{g}{ik}\right)t, \\
t &= \frac{1}{\left(1 + \frac{ig}{2k}\right)}, \quad r = -i \frac{g}{2k} t, \quad |t|^2 + |r|^2 = 1.
\end{aligned} \tag{B4}$$

$$S^\dagger = \begin{pmatrix} r^\dagger & t^\dagger \\ t'^\dagger & r'^\dagger \end{pmatrix} = \begin{pmatrix} [r - t' r'^{-1} t]^{-1} & -[r - t' r'^{-1} t]^{-1} t' r'^{-1} \\ -r'^{-1} t [r - t' r'^{-1} t]^{-1} & [r' - t r^{-1} t']^{-1} \end{pmatrix}, \tag{B9}$$

$$r^{\dagger^{-1}} = r - t' r'^{-1} t, \quad t'^{\dagger^{-1}} = t' - r t^{-1} r'. \tag{B10}$$

Consistency of Eq. (B8) can be easily seen in the case of a single channel with $t = t'$ for time-reversal invariance. From unitarity,

$$\frac{r}{r'^*} = -\frac{t}{t'^*}, \tag{B11}$$

so that, if we substitute this into Eq. (B10) we get

$$r - r^{*-1} = -r^{*-1} t t^*, \quad r^{*-1} = r [1 - t t^*]^{-1}, \tag{B12}$$

$$t^{*-1} - t = r^* r t^{-1} t t^{*-1}, \quad [1 - r^* r] t^{*-1} = t. \tag{B13}$$

As $r^* r + t t^* = 1$, the second of Eq. (B13) is $t = t$, while the second of Eq. (B12) is satisfied by $r = t - 1$ if $t = 1/(1 + i \frac{\kappa_+}{2k})$. The result is

$$t = \frac{1}{1 + \frac{i \kappa_+}{2k}}, \quad r = t - 1 = -\frac{i \kappa_+}{2k} t, \tag{B14}$$

which is what is found in case of a δ -function potential.

APPENDIX C: SIGNATURE OF THE PAIR-BREAKING PROCESSES IN THE DIELECTRIC FUNCTION AT $k_0 = \frac{2\Delta}{\hbar c}$

An approximate comparison between $\epsilon_1(\omega)$ for the normal and the superconducting phases is reported in Fig. 2.

We use Eq. (B3) together with Eqs. (B1) and (B2) to derive the dependence of α, β on κ_L, κ_R, k ($\kappa_+ = \kappa_L + \kappa_R$):

$$\begin{aligned}
r &= (\alpha + \beta) \cos \theta, \quad s = \tau = (\alpha - \beta) \sin \theta, \\
1 - t &= -(\alpha + \beta) \cos \theta,
\end{aligned} \tag{B5}$$

$$\begin{aligned}
-2ik(\alpha + \beta) &= g[V(1 + \alpha) - V^*\beta], \\
\kappa_+(\alpha - \beta) &= g[V\alpha + V^*\beta].
\end{aligned} \tag{B6}$$

Solving Eq. (B6) with respect to α, β , we get, to lowest order in g ,

$$\alpha + \beta = \frac{gV}{2\kappa_+} \left[1 + \frac{\kappa_+}{2ik}\right], \quad \alpha - \beta = \frac{gV}{2\kappa_+} \left[1 - \frac{\kappa_+}{2ik}\right]. \tag{B7}$$

κ should depend on the interaction \hat{V} , but, in the absence of information about the interaction \hat{V} , we take it as a function of the κ 's themselves. We take

$$\frac{gV}{2\kappa_+} = -i \frac{\kappa_+}{2k} \frac{1}{1 + \left(\frac{\kappa_+}{2|k|}\right)^2}. \tag{B8}$$

This choice is consistent with unitarity of the S matrix which implies $S^\dagger = S^{-1}$:

According to Eq. (4) and the arguments given above, the two functions should acquire the same functional behavior at very low temperature, both at low and high frequencies, if the metal is assumed close to being ideal.

At very low temperature and frequency the difference is very small, due to the contribution of the δ function at zero frequency to the Kramers-Kronig transform of Eq. (2), with $\omega_{ps} \approx \omega_p$. In fact, the δ zero-frequency peak of the superconducting phase provides $\epsilon(\omega)$ given by Eq. (4), which is the same as in the case of an ideal normal metal (with $\omega\tau \gg 1$). Increasing the temperature the quasiparticles contributing to the normal metal phase are absent in the superconductor, inside the energy gap, and a difference emerges. In Fig. 2 we report the difference between the superconducting and normal metal response at microwave frequency, which vanishes at zero temperature well below $2\Delta/\hbar$. The sharp peak at $\omega \sim 2\Delta/\hbar$ heralds the enhancement of QP excitations at the pair-breaking energy. Correspondingly, there is a dip in the mode dispersion of the superconducting phase, as compared to the normal phase, which is concentrated at the pair-breaking frequency $\omega\tau = 2$. This can be seen by comparing the two equations derived from Eq. (11) for the symmetric mode, between the normal and superconducting case:

$$-\epsilon_S(\omega_S) = \frac{\kappa_S}{\kappa_0} \coth \frac{\kappa_S a}{2}, \quad -\epsilon_N(\omega_N) = \frac{\kappa_N}{\kappa_0} \coth \frac{\kappa_N a}{2}.$$

If we neglect retardation in this frequency range, $\kappa_S \approx \kappa_N \approx \kappa_0 = k_{||}$, so that, with $\epsilon_S(\omega_S) \approx \epsilon_S(\omega_N) + \delta\omega \left. \frac{\partial \epsilon_S(\omega)}{\partial \omega} \right|_{\omega_N}$, we

observe that

$$\epsilon_S(\omega_N) - \epsilon_N(\omega_N) + \delta\omega \left. \frac{\partial \epsilon_S(\omega)}{\partial \omega} \right|_{\omega_N} = 0. \quad (C1)$$

Immediately before the peak, the difference is positive and the derivative is positive, so that $\delta\omega < 0$. Immediately after the peak, the derivative becomes negative so that $\delta\omega > 0$ and

they form a cusp pointing downward. After the peak, the difference is negative and the derivative is positive, so that $\delta\omega > 0$ increases again. The location of the cusp is about $k_0 = \frac{2\Delta}{\hbar v}$ where $v \sim 10^8$ cm/s is the velocity of the electron in the metal, giving $k_0 = 250$ (μm)⁻¹ which is a k vector sampling distances of the order of the lattice spacing, beyond the validity of this approach.

-
- [1] R. P. Feynman, R. B. Leighton, and M. Sands, *The Feynman Lectures on Physics: The Ambiguity of the Field Energy* (Addison-Wesley, Reading, MA, 1966), Vol. 2, p. 27-4.
- [2] S. Avino *et al.*, Progress in a Vacuum Weight Search Experiment, *Physics* **2**, 1 (2020).
- [3] E. Calloni, M. De Laurentis, R. De Rosa, F. Garufi, L. Rosa, L. Di Fiore, G. Esposito, C. Rovelli, P. Ruggi, and F. Tafuri, Towards weighing the condensation energy to ascertain the Archimedes force of vacuum, *Phys. Rev. D* **90**, 022002 (2014).
- [4] A. Allocca, G. Bimonte, D. Born, E. Calloni, G. Esposito, U. Huebner, E. Il'ichev, L. Rosa, and F. Tafuri, *J. Supercond. Novel Magn.* **25**, 2557 (2012).
- [5] S. Léger, J. Puertas-Martínez, K. Bharadwaj, R. Dassonneville, J. Delaforce, F. Foroughi, V. Milchakov, L. Planat, O. Buisson, C. Naud *et al.*, Observation of quantum many-body effects due to zero point fluctuations in superconducting circuits, *Nat. Commun.* **10**, 5259 (2019).
- [6] A. Kempf, On the Casimir effect in the high-Tc cuprates, *J. Phys. A: Math. Theor.* **41**, 164038 (2008).
- [7] P. W. Anderson, *Phys. Rev.* **110**, 827 (1958).
- [8] P. W. Anderson, *Phys. Rev.* **130**, 439 (1963).
- [9] J. W. Negele and H. Orland, *Quantum Many-Particle Systems*, Frontiers in Physics (Addison-Wesley, Reading, MA, 1987).
- [10] M. Bordag, The Casimir effect for thin plasma sheets and the role of the surface plasmons, *J. Phys. A: Math. Gen.* **39**, 6173 (2006).
- [11] A. Allocca, S. Avino, S. Balestrieri, E. Calloni, S. Caprara, M. Carpinelli, L. D'Onofrio, D. D'Urso, R. De Rosa, L. Errico *et al.*, *Eur. Phys. J. Plus* **137**, 826 (2022).
- [12] A. J. Berlinsky, C. Kallin, G. Rose, and A.-C. Shi, *Phys. Rev. B* **48**, 4074 (1993).
- [13] R. E. Glover, III and M. Tinkham, *Phys. Rev.* **108**, 243 (1957).
- [14] D. C. Mattis and J. Bardeen, *Phys. Rev.* **111**, 412 (1958).
- [15] K. Holczer, O. Klein, and G. Grüner, *Solid State Commun.* **78**, 875 (1991).
- [16] O. Klein, E. J. Nicol, K. Holczer, and G. Grüner, *Phys. Rev. B* **50**, 6307 (1994).
- [17] B. B. Jin, T. Dahm, A. I. Gubin, Eun-Mi Choi, H. J. Kim, Sung-IK Lee, W. N. Kang, and N. Klein, *Phys. Rev. Lett.* **91**, 127006 (2003).
- [18] K. Steinberg, M. Scheffler, and M. Dressel, *Phys. Rev. B* **77**, 214517 (2008).
- [19] K. Saermark, *J. Phys. F: Met. Phys.* **7**, 2109 (1977).
- [20] M. M. Doria, G. Hollauer, F. Parage, and O. Buisson, *Phys. Rev. B* **56**, 2722 (1997).
- [21] A. J. Annunziata, D. F. Santavicca, L. Frunzio, G. Catelani, M. J. Rooks, A. Frydman, and D. E. Prober, *Nanotechnology* **21**, 445202 (2010).
- [22] J. E. Mooij and G. Schön, *Phys. Rev. Lett.* **55**, 114 (1985).
- [23] M. Bordag, U. Mohideenb, and V. M. Mostepanenko, *Phys. Rep.* **353**, 1 (2001).
- [24] P. W. Anderson, *Phys. Rev.* **112**, 1900 (1958).
- [25] M. Minutillo, D. Giuliano, P. Lucignano, A. Tagliacozzo, and G. Campagnano, *Phys. Rev. B* **98**, 144510 (2018).
- [26] R. Guérout, G.-L. Ingold, A. Lambrecht, and S. Reynaud, *Symmetry* **10**, 37 (2018).
- [27] C. I. Sukeik, M. G. Boshier, D. Cho, V. Sandoghdar, and E. A. Hinds, *Phys. Rev. Lett.* **70**, 560 (1993).
- [28] G. Bimonte, E. Calloni, G. Esposito, L. Milano, and L. Rosa, *Phys. Rev. Lett.* **94**, 180402 (2005).
- [29] G. Bimonte, E. Calloni, G. Esposito, and L. Rosa, *Nucl. Phys. B* **726**, 441 (2005).
- [30] G. Bimonte, B. Detlef, E. Calloni, G. Esposito, U. Hubner, E. Il'ichev, L. Rosa, O. Scaldaferrri, F. Tafuri, and R. Vaglio, *J. Phys. A: Math. Gen.* **39**, 6153 (2006).